University of Groningen
Kapteyn Astronomical Institute

NOVA Optical and Infrared Group

Characterizing the transmission of three MICADO filters at cryogenic and room temperatures

Author: Valeria Tarsina

Supervisors:
Joost van den Born (NOVA)
Ester Aranzana (NOVA)
Eline Tolstoy (Kapteyn Astronomical Institute)

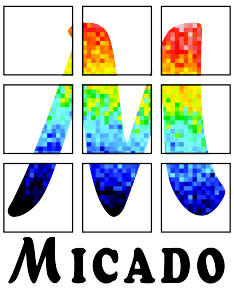

July 10, 2025

Abstract

MICADO (Multi-AO Imaging Camera for Deep Observations) is an adaptive optics instrument designed for high resolution imaging at near-infrared wavelength and it will be deployed in 2030 on the Extremely Large Telescope (ELT). MICADO will feature a wide range of filters, masks and stops that will operate at a temperature of 82 K. The filters and their corresponding samples are coated by the companies Cilas and SCHOTT according to the requirements defined by NOVA. Two filters of each specific kind were coated to ensure that one could serve as a spare. This report focuses on measuring the transmission of the [FeII], H-continuum and I-long filters at room (293 K) and cryogenic (84 K and 100 K) temperatures in order to asses their performance. The measurements show that the transmission curves shift towards shorter wavelengths at lower temperatures. We determined that both [FeII] filters comply with the specifications and they will be accepted. One of the H-continuum filters does not comply with the requirements and hence, it will be kept as a spare, while the other will be integrated in MICADO. The I-long filters showed a large number of coating defects, which could lead to stray light effects that, in turn, might affect photometry and high contrast imaging. Thus, it was decided to reject these two filters, even if the transmission curve of the sample satisfied the requirements. At the time of writing this thesis, wavefront error measurements are being conducted as part of the final acceptance process of the filters.

Contents

Acronyms

ADC Atmospheric Dispersion Corrector

AGN Active Galactic Nucleus

AO Adaptive Optics

AoI Angle of Incidence

AR Anti-reflection

as arcsecond

CRiSP CRyostat in SPectrometer

CWL Central wavelength

CWM Central Wheel Mechanism

ELT Extremely Large Telescope

ESO European Southern Observatory

FoV Field of View

FTS Fourier Transform Spectrometer

FWM Filter Wheel Mechanism

HST Hubble Space Telescope

JWST James Webb Space Telescope

MCAO Multi-conjugate adaptive optics

MICADO Multi-Adaptive Optics Imaging Camera for Deep Observations

MORFEO Multiconjugate adaptive Optics Relay For ELT Observations

NIR Near-infrared

NOVA Nederlandse Onderzoekschool voor Astronomie (Netherlands Research School for Astronomy)

PWM Pupil Wheel Mechanism

SCAO Single-conjugate adaptive optics

UV Ultraviolet

VLT Very Large Telescope

WFE Wavefront error

Chapter 1

Introduction

During an experiment performed in 1800, William Herschel determined that thermometers placed beyond the visible red spectrum showed a higher temperature than those in the visible range (e.g. Minkina, 2021). This led to the discovery of infrared radiation, which marked the beginning of a new era for Astronomy. Unlike visible light, infrared radiation can penetrate through dust clouds, allowing observations of star-forming regions and obscured galactic centers, providing insights into both stellar evolution and supermassive black holes activity (e.g. Beckman, 2021).

The need for high resolution imaging of stars and active galactic nuclei, combined with the rapid technological advancements over the past decades, enabled scientists and engineers to build larger telescopes such as the Very Large Telescope (VLT) and the James Webb Space Telescope (JWST). This trend can be attributed to the relation between the optical resolution and the diameter of a telescope

$$\theta \propto \frac{\lambda}{D}, \tag{1.1}$$

where θ is the minimum resolvable angular separation, λ is the light's wavelength and D is the diameter of the mirror (Hecht, 2017). In order to resolve smaller objects, the value of θ has to be reduced, which can be achieved by increasing the diameter, hence the desire to build larger telescopes on Earth.

1.1 The Extremely Large Telescope

The Extremely Large Telescope (ELT) represents a new advance in technological development, aiming to capture deeper and higher resolution images of the Universe. This project is led by the European Southern Observatory (ESO), which started building the facility in 2014 at Cerro Armazones in the Atacama Desert in Chile. This location was selected due to its high altitude (3064 meters) and dry climate, where the water vapor is minimal and the skies are clear for almost the entire year, making it a favorable place for observations both in the visible and infrared ranges. ELT has five mirrors, with the primary measuring 39 meters, making it the largest ground–based optical–infrared telescope in the world (Padovani & Cirasuolo, 2023). Currently, the highest point of the dome has been reached and the panels

that will protect the mirrors and the instruments are being installed (see Figure 1.1).

The ELT will have several instruments with capabilities for imaging, spectroscopy and astrometry at different wavelengths. Adaptive Optics (AO) will play a crucial role in enabling high spatial resolution performance by correcting for atmospheric distortions that otherwise limit the resolving power. ELT will be equipped with powerful lasers that act as guide stars, as seen in Figure 1.2, allowing for observations at any position on the sky (Padovani & Cirasuolo, 2023). The first light instruments are MICADO, which will take deep images at near-infrared (NIR) wavelengths (Davies et al., 2016) and METIS – a spectrograph and imager that will operate in mid-infrared (Brandl et al., 2021). The next generation of instruments will be HARMONI – a visible and NIR integral field spectrograph (Muslimov et al., 2024), MORFEO – a multi-conjugate adaptive optics system, MOSAIC — a multi object spectrograph, and ANDES – a high Dispersion Echelle Spectrograph. Currently, ELT is under construction and the daily progress can be monitored by the public via this link provided by ESO. It is expected that MICADO and METIS will be integrated in 2030.

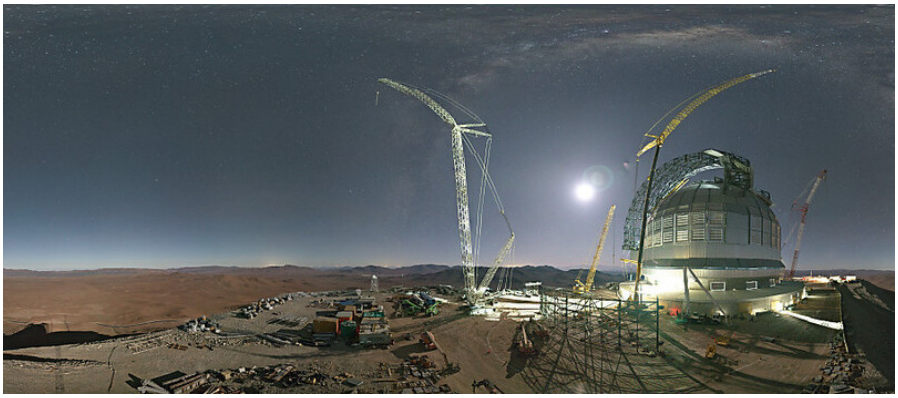

Figure 1.1: The state of ELT's dome on the 20th May 2025. Retrieved from ESO, 2025.

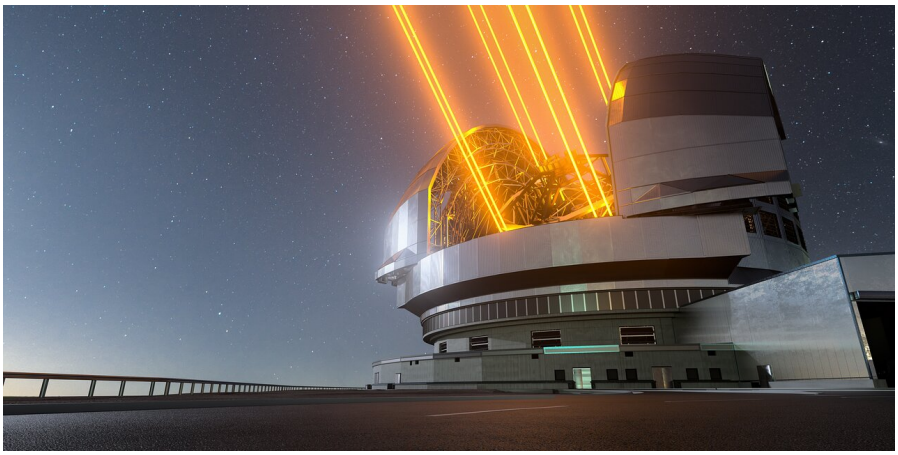

Figure 1.2: Artist impression of the ELT's dome and its lasers used as artificial guide stars in order to correct for atmospheric distortions. Retrieved from ESO, 2020b.

1.2 MICADO

MICADO is the Multi-Adaptive Optics Imaging Camera for Deep Observations (see Figure 1.3) that will be used to take images in the NIR range at wavelengths between 0.8 and 2.4 µm. Initially, MICADO will operate as a stand alone instrument by employing single-conjugate adaptive optics (SCAO), which uses a single natural guide star for wavefront sensing. This module will enable high resolution zoomed imaging, but with increasing angular distance from the guide star, the quality of the images deteriorates (van den Born, 2023; Vidal et al., 2022). To enlarge the field of view (FoV), the multi-conjugate adaptive optics (MCAO) module, MORFEO, will be introduced at a later stage, enabling the full capacity of MICADO by correcting for the atmospheric turbulence with the aid of three natural guide stars and six lasers along with multiple deformable mirrors (Ciliegi et al., 2022).

For MICADO, a total of three modes will be available for various types of astronomical measurements and one mode will be used to perform calibrations. They can be achieved by switching the filters, masks and the selection mechanisms shown in Figure 1.4. The zoomed imaging mode will make use of a three-mirror anastigmat with four mirrors placed between, creating the configuration known as High Resolution Imager (HRI). It will enable a FoV of $\sim 20 \times 20$ arcseconds with 1.5 mas per pixel. The Low Resolution Imager (LRI) requires two fold mirrors to move in. This mode covers a FoV of $\sim 54 \times 54$ arcsec at a scale of 4 mas per pixel and will be used for imaging at high spatial resolution and astrometric imaging. Lastly, the users will be able to perform spectroscopy to obtain high resolution spectra of compact sources using two echelle gratings. A pupil imaging mode is available for calibration purposes by employing two flat fold mirrors and a lens (Davies and Sturm, 2021; van den Born, 2023).

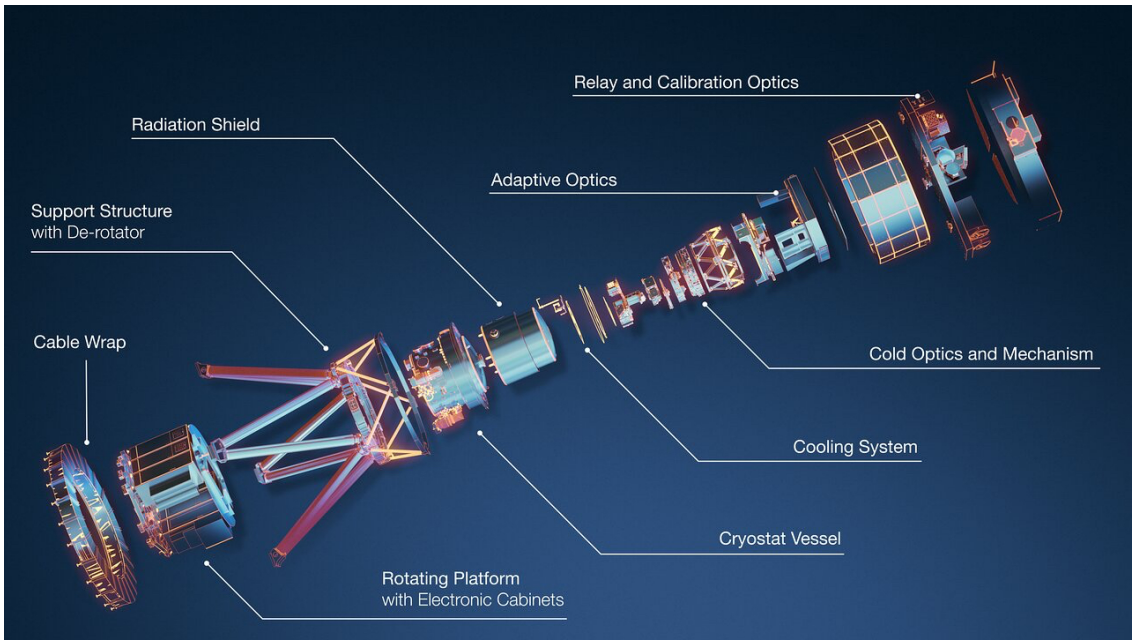

Figure 1.3: Exploded view of MICADO, showing its components. The instrument will be 6 meters tall and will weigh 20 tonnes. Retrieved from ESO, 2024.

As MICADO is an IR instrument, its optical components need to be cooled down to 77K by placing them inside a large cryostat (see Figure 1.4), as described in more detail by Janssen et al., 2021 and van den Born, 2023. Before entering the cryostat, the light passes through a series of optics that perform multiple corrections of the incoming light. The MICADO Calibration Assembly (MCA) will take flat fields and ensure that the instrument is well calibrated. The Relay Optics (RO) will be used to guide the light towards SCAO and it will act as a placeholder for MORFEO until its deployment. The Single Conjugate Adaptive Optics (SCAO) will measure the wavefront of light coming into the instrument, while LOR will be a Low Order Reference wavefront sensor for the natural guide stars that can be both inside and outside the instrument's FoV (Davies & Sturm, 2021). Inside the cryostat, the light first passes through the collimator optics that align the incoming rays. Later, the beam will go through the Central Wheel Mechanism (CWM) consisting of the Atmospheric Dispersion Corrector (ADC), the Filter Wheel Mechanism (FWM) and the Pupil Wheel Mechanism (PWM). The ADC will compensate for the atmospheric differential refraction using two counter rotating double prisms that adjust the dispersion effects based on the zenith angle. The FWM consists of two wheels that will host around thirty filters, which include broad band filters, spectroscopic order sorting filters and neutral density filters. The PWM will accommodate masks, narrow band filters and stops. Lastly, the camera optics project the beam onto the detector, creating an image (van den Born, 2023, Janssen et al., 2021).

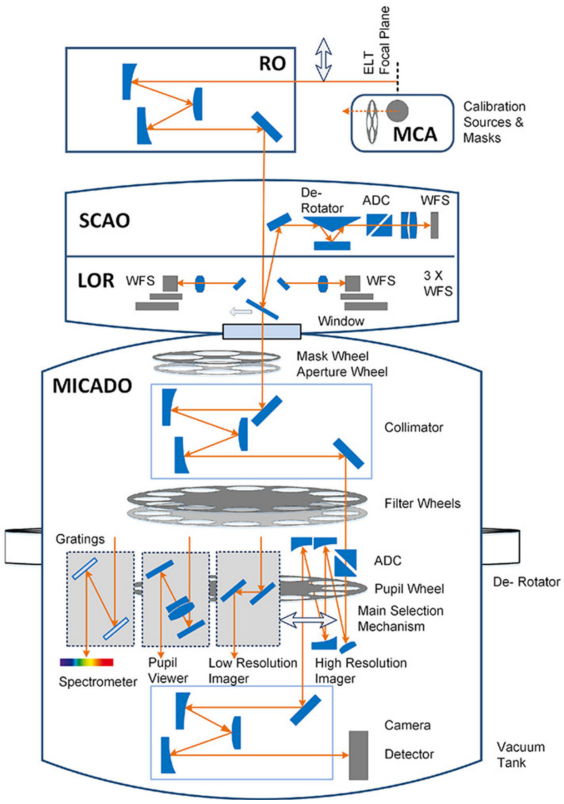

Figure 1.4: Schematic drawing of the MICADO optics inside the cryostat and the AO module on top of it. Retrieved from ESO, 2020a.

1.3 The scientific cases behind MICADO's development

MICADO represents a significant advancement in our ability to observe the Universe with a level of detail that is not possible using current instruments. Thanks to the large collecting area of the ELT's primary mirror which has a 39 meter diameter, MICADO will be able to achieve high resolution images that will make it possible to detect faint and compact objects. For example, this allows the study of high-redshift galaxies to gain insights into the early stages of galaxy formation and evolution. Due to the ability of resolving structures smaller than 100 pc at high redshifts, MICADO will study the formation and evolution of both galaxies and star clusters at greater distances than currently possible, revealing their composition and age. Closer by, we will be able to observe individual stars in nearby galaxies, which will allow us to learn in more detail their formation history (Davies et al., 2016). Moreover, MICADO will be able to look at the motion of the stars in the vicinity of the super massive black hole Sagittarius A* in the center of our Galaxy, offering a deeper understanding of AGN feedback and the phenomena of matter accretion (Padovani & Cirasuolo, 2023). MICADO will also enable the study of the atmospheres and weather in the planets from our Solar System, as well as exoplanets, potentially leading to identification of a greater abundance of molecules that can sustain life (Padovani & Cirasuolo, 2023). Two simulations that compare the resolution of MICADO to that of HST, JWST and VLT are presented in Figures 1.5 and 1.6.

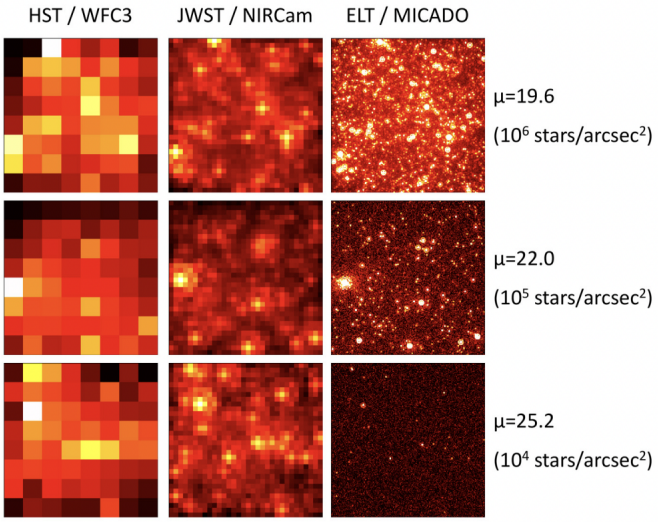

Figure 1.5: Simulated observations showing how a crowded stellar region would be seen by HST (left column), JWST (middle column) and ELT's instrument MICADO (right column). The bottom row represents the stellar density at a radius of 4-5$R_{\rm eff}$ for NGC 4472 in the Virgo Cluster, which is the limit of JWST. The row on the top represents 2$R_{\rm eff}$ within the same galaxy, where MICADO is still able to resolve many individual stars. The size of each panel is 1 arcsecond. Retrieved from Davies et al., 2021.

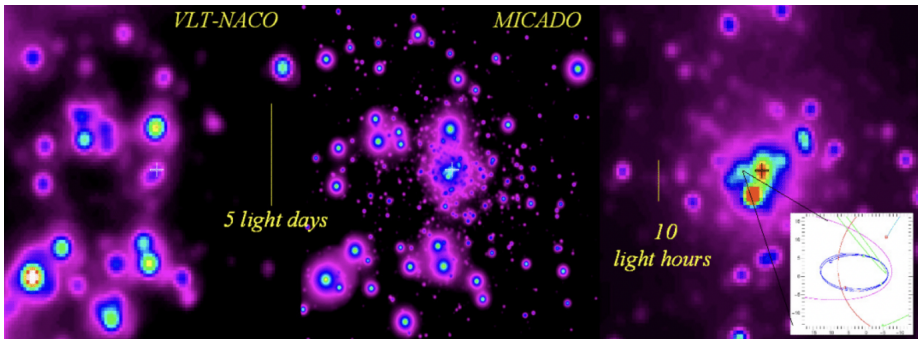

Figure 1.6: The stars orbiting around Sagittarius A* black hole observed by VLT–NACO with a resolution of 60 mas on the left. In the middle, a simulation based on the VLT image shows how the stars would appear when observed with MICADO. On the right, the central region of the MICADO image is zoomed in for greater detail. Retrieved from Renzini, Davies, et al., 2009.

1.4 NOVA's role within the MICADO Consortium

MICADO is developed and built by a consortium which includes institutions from Germany, the Netherlands, France, Austria, Finland and Italy and it is led by the Max Planck Institute for Extraterrestrial Physics (MPE). NOVA is responsible for designing, manufacturing, integrating and testing the CWM and the ADC, along with verification and validation of the bandpass filters coated by the companies SCHOTT and Cilas. The CWM was successfully tested both in warm and cryogenic environments in March 2025 at MPE in Munich and now it is stored at NOVA Dwingeloo (see Figures 1.7 and 1.8). Starting May 2025, SCHOTT and Cilas began delivering the filters, which are being inspected and their cryogenical performance is measured to verify their transmission and wavefront errors.

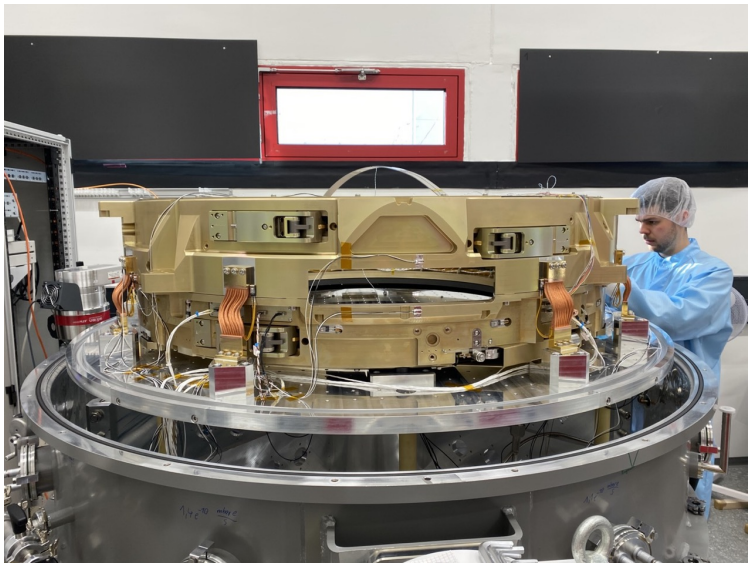

Figure 1.7: CWM integrated in the test cryostat at the MPE lab in Munich in March 2025.

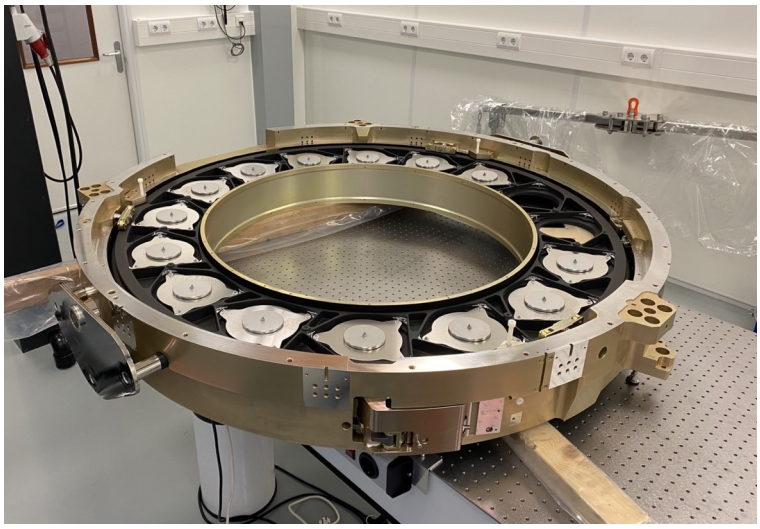

Figure 1.8: The assembly stage of the FWM in the clean room of NOVA. Dummy masses are used to mimic the filters in order to avoid potential issues such as debris coming from other components.

1.4.1 My contribution within the MICADO team

One of NOVA's responsibilities is testing and validating the filters that are going to be used in the FWM and the PWM. During my 3 months internship at NOVA, I had the task to research the theory behind thin-film filter coatings to gain deeper understanding of their properties (chapter 2). I familiarized myself with the reasoning behind the choice of the MICADO filters by getting acquainted with the science case documents and considering inputs from Eline Tolstoy, who is also the Project Scientist of the instrument (chapter 3). With the guidance and help of my main supervisor, Joost van den Born, I performed a visual inspection of the I-long, [FeII] and H-cont filters in NOVA's clean room. Cilas and SCHOTT provided two samples (hereafter referred to as witness samples), measuring 25 mm, for each filter set. We integrated them in a cryostat in order to perform transmission measurements with the spectrometer available in the optics lab (chapter 4). Using the gained knowledge about the desired specifications of the filters, I compared the empirical data to the documented requirements in order to asses the filters' performance at room temperature and in cryogenic environments (chapter 5). Ester Aranzana coordinated the schedule, maintained close communication with the companies supplying the filters and guided me through the process of writing this thesis.

Chapter 2

Theory of filter coatings

To achieve the desired performance of various optical surfaces, such as filters and camera lenses, specialized coatings have been developed in order to remove the unwanted reflections and improve optical efficiency. The most common way to attain high transmittance is by stacking thin film layers on optical substrates to produce destructive interference patterns, or to reflect the undesired light so that only certain wavelengths can pass through. This method involves depositing from a few to a hundred layers with varying thickness and properties to meet different design specifications (Hecht, 2017, Dobrowolski, 1978).

2.1 Antireflection coatings and quarter-wave stacks

Thin film coatings rely on the principle of interference between light waves reflected at the upper and lower boundaries of a film layer. As a beam of light hits a film layer, part of it is reflected from the top surface, while the rest continues through the film and reflects from the bottom surface. Afterwards, the two resulting beams recombine in two ways. If their relative phase shift is 180°, their amplitudes subtract, meaning that they interfere destructively. If the shift is zero or a multiple of 360°, then their amplitudes add and the beams interfere constructively. This process occurs at every interface throughout the stack and the reflected light is a combination of all the resulting beams, as seen in Figure 2.1.

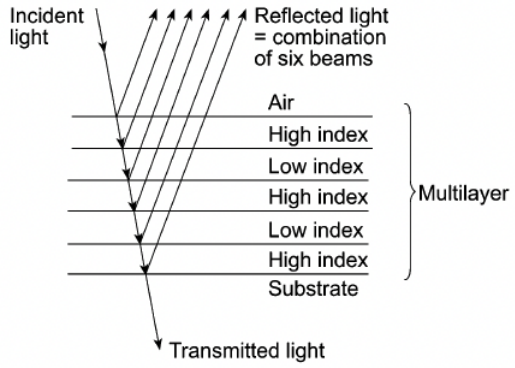

Figure 2.1: Propagation of light through a multilayer thin film stack. Retrieved from Macleod, 2001.

In order to maximize the transmittance of a thin film filter, the reflection of light can be reduced using anti-reflection (AR) coating materials. Their goal is to ensure that the light reflected at the upper and lower surfaces of a thin film layer is canceled. For this to occur, two conditions need to be satisfied. First, the amplitudes of the reflected light from the top and bottom surfaces of the film layer must be equal, implying that the refractive index of the coating, n_c, needs to satisfy the relation

$$n_c = \sqrt{n_0 \cdot n_s}, \tag{2.1}$$

where n_0 is the refractive index of the incident medium (e.g. air) and n_s is the refractive index of the substrate (e.g. glass). Second, the two reflected beams from a layer must interfere destructively, which is ensured by introducing a 180° phase shift. This is achieved by stacking, on top of the substrate, pairs of alternating high and low refractive index thin film layers with the optical thickness equal to a quarter of the central wavelength around which the filter is designed. This structure is known as a quarter-wave stack and it is represented as

$$a(LH)^m g,$$

where a and g stand for the refractive indices of air and glass, H and L represent the layers with high and low refractive indices and, m indicates the number of repeated (HL) pairs (Macleod, 2001; Hecht, 2017).

AR quarter-wave stack coatings are not designed using a fixed method. Instead, the process typically involves experiments and automated computer calculation, but it can also be performed analytically using approximations, as I will explain and illustrate in the following sections.

2.2 Thin film interference coatings

Consider a beam of light traveling through air that is incident at an angle θ on the surface of a thin film coating consisting of m layers. Part of the electromagnetic radiation is reflected multiple times within the system, while the rest is transmitted through each layer at an angle ϕ_j, with $j = (1, 2, .., k)$, until reaching the glass substrate, as depicted in Figure 2.2. The material of each layer can vary and, consequently, each film is characterized by a different refractive index n_j and optical thickness d_j (Dobrowolski, 1978). The optical thickness of a layer results in an optical path length proportional to a quarter wavelength and it is computed via the relation (Peatross & Ware, 2023)

$$d_j = \frac{\lambda_0}{4n_j \cos \phi_j}, \tag{2.2}$$

where λ_0 is the central wavelength of the filter and ϕ_j is the propagation angle of light through the jth layer.

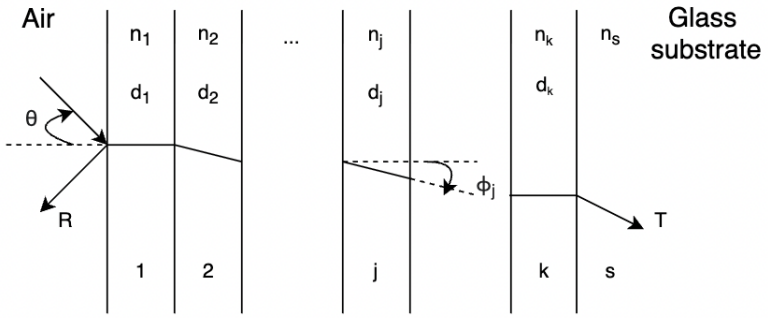

Figure 2.2: The structure of a multilayer coating and the propagation of light inside it. Adopted from Dobrowolski, 1978.

In order to compute the transmittance and reflectance of a multilayer coating, we will make use of the concept of characteristic matrices as described by Dobrowolski, 1978 and Hecht, 2017. The fundamental condition that needs to be satisfied is that the tangential component of the electric field ($\vec{\boldsymbol{E}}$) and the magnetic field ($\vec{\boldsymbol{H}} = \vec{\boldsymbol{B}}/\mu$) must be continuous at the boundaries of two thin film surfaces. This allows to obtain a linear relation between two consecutive layers using a characteristic matrix M, which relates the electromagnetic fields at two neighboring interfaces. For instance, at the boundary between the first and second layer, the continuity of the tangential electric and magnetic fields can be written as

$$\begin{bmatrix} E_1 \\ H_1 \end{bmatrix} = M_1 \begin{bmatrix} E_2 \\ H_2 \end{bmatrix}, \tag{2.3}$$

with M_1 being the characteristic matrix corresponding to the first layer. For a multilayer coating, the characteristic matrices are multiplied consecutively, up to the final layer. The relationship between the first and the last boundaries can then be expressed as

$$\begin{bmatrix} E_1 \\ H_1 \end{bmatrix} = M_1 M_2 ... M_k \begin{bmatrix} E_s \\ H_s \end{bmatrix} = \begin{bmatrix} m_{11} & m_{12} \\ m_{21} & m_{22} \end{bmatrix} \begin{bmatrix} E_s \\ H_s \end{bmatrix}, \tag{2.4}$$

where the subscript k denotes the last layer and s refers to the substrate, while $m_{11}, m_{12}, m_{21}, m_{22}$ are the components of the total characteristic matrix resulting from the multiplication of the inidividual layer matrices. The characteristic matrix of the jth film can be expressed by a 2×2 matrix

$$M_j = \begin{bmatrix} \cos\delta_j & i\frac{\sin\delta_j}{Y_j} \\ iY_j \sin\delta_j & \cos\delta_j \end{bmatrix}, \tag{2.5}$$

where i is a complex number and

$$\delta_j = \frac{2\pi}{\lambda_0}(n_j d_j \cos\phi_j) \tag{2.6}$$

represents the extra distance traveled by the wave through a film layer due to the propagation angle ϕ_j, the layer's refractive index n_j and its optical thickness d_j. This quantity is also

known as phase shift or optical path difference.

Y_j from Equation (2.5) is the effective index of refraction and it depends on the polarization state of the incident radiation – perpendicular or parallel and is written as

$$Y_j = \begin{cases} \frac{n_j}{\cos\phi_j}, & \text{for p-polarized light (parallel)} \\ n_j \cos\phi_j, & \text{for s-polarized light (perpendicular)} \end{cases}. \tag{2.7}$$

In order to find the propagation angle ϕ_j, we begin by applying Snell's law between air, with the refractive index $n_0 = 1$, and the first layer, which yields

$$n_0 \sin\theta = n_1 \sin\phi_1, \tag{2.8}$$

with θ being the angle of incidence (AOI). The law is applied between every two consecutive coating layers, using the corresponding refractive indices and propagation angles, until reaching the substrate.

Having collected the necessary elements and performing a series of derivations presented in detail by Hecht, 2017, the transmission coefficient is computed as

$$t = \frac{2Y_0}{Y_0 m_{11} + Y_0 Y_s m_{12} + m_{21} + Y_s m_{22}}, \tag{2.9}$$

where Y_0 and Y_s are based on Equation (2.7) and stand for the effective refractive indices of air and glass. Finally, the transmittance can be computed as

$$T = \frac{n_0}{n_s}|t|^2, \tag{2.10}$$

where we remind the reader that n_0 and n_s are the refractive indices of air and glass, respectively.

2.3 Simulation of a bandpass filter

In order to illustrate the theoretical concept derived in the previous section, a simulation of a bandpass filter in Python was performed. An example recipe for obtaining high transmittance with alternating high (H) and low (L) refractive index films is (Dobrowolski, 1978)

$$a\{[(0.5H)L(0.5H)]^3 H[(0.5H)L(0.5H)]^3\}^N g.$$

This multilayer stack starts in air and ends in glass. The alternation $(0.5H)L(0.5H)$ is repeated three times, followed by a full high index layer H and then another repetition of the sequence $(0.5H)L(0.5H)$ for three times. The whole structure is repeated N times. It is also important to mention that in the case of a quarter-wave stack, the thickness of the H-layers will become $\frac{\lambda_0}{8}$, except for the high index layer in the middle.

To design an I-band filter centered at $\lambda_0 = 867$ nm, first consider the case where the light

hits the first layer of the stack at normal incidence, so $\theta = 0°$ and it is s-polarized. From Equations (2.2) and (2.6), we see that the refractive index of the coating impacts the optical thickness length, which in turn influences the phase shift. To illustrate this, I generate a theoretical transmittance curve for two cases (see Figure 2.3):

1. the high and low refractive indices of the thin films are close in value;
2. the high and low refractive indices of the thin films differ significantly.

For both cases, I chose antireflection coating materials with low and high refractive indices, denoted by n_L and n_H respectively. I use the same low index material with $n_L = 1.35$, corresponding to Na_3AlF_6, for both simulations, while varying the high-index material. For the first case, the chosen value for the high refractive index material is $n_H = 1.46$, which corresponds to SiO_2, and for the second case, I picked a Ta_2O_5 coating with $n_H = 2.1$. Note that the shape of the curve is influenced by the amount of repetitions of the sequence, denoted by N. The highest transmittance is achieved using $N = 3$ for case 1 and $N = 2$ for case 2.

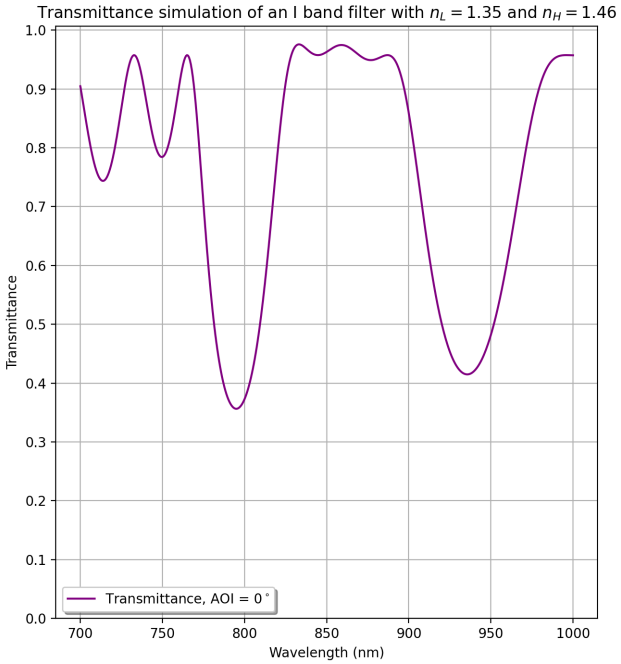

(a) Theoretical transmittance curve for films with refractive indices that are close in value.

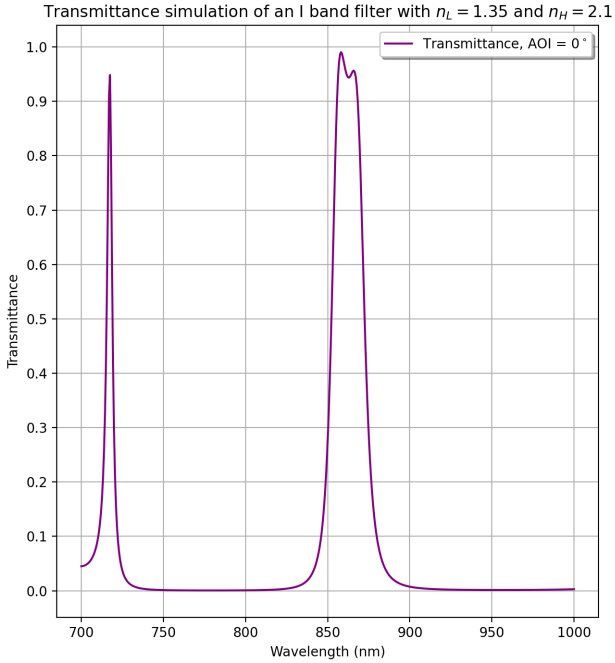

(b) Theoretical transmittance curve for thin films with refractive indices that differ significantly.

Figure 2.3: Effect of varying refractive indices in multilayer coatings on transmittance.

As seen in Figure 2.3a, when the refractive indices of the two coatings are closer in value, the transmission range gets broader, spanning over approximately 125 nm, compared to a 50 nm width in the second case depicted in Figure 2.3b. The transmittance does not reach values lower than 0.36% for case 1, but this can be solved by applying extra layers of different materials or by introducing cavities (Dobrowolski, 1978). Yet, the simulation of case 1 matches closely the actual properties of MICADO's I-long filter which will be described later

in this report. In order to find the central wavelength λ_0, I take the transmission weighted mean of the wavelengths given by (Sivia & Skilling, 2006)

$$\lambda_0 = \frac{\sum_{i=1}^{n} \lambda_i T(\lambda_i)}{\sum_{i=1}^{n} T(\lambda_i)}, \tag{2.11}$$

with λ_i standing for the ith wavelength value and $T(\lambda_i)$ is the correspoding transmittance. The obtained central wavelengths are $\lambda_0 = 863.69$ nm for case 1 and $\lambda_0 = 864.03$ nm for case 2, which deviate by approximately 3 nm from the chosen central wavelength $\lambda_0 = 867$ nm. By applying more complex AR coatings, we can achieve values closer to λ_0.

In addition to the passbands of interest, both plots from Figure 2.3 show multiple high transmission regions, which are not ideal for scientific use. The problem could be tackled by either using a high-pass filter in order to block the other transmitting areas or by making the detector not sensitive outside the desired wavelength range (Dobrowolski, 1978).

Furthermore, I examined how the angle of incidence (AOI) influences the transmission region (see Figure 2.4). For simplicity, I implemented the change only on the case 2 filter, with films that have very different refractive indices. The behavior is the same for the other simulated filter.

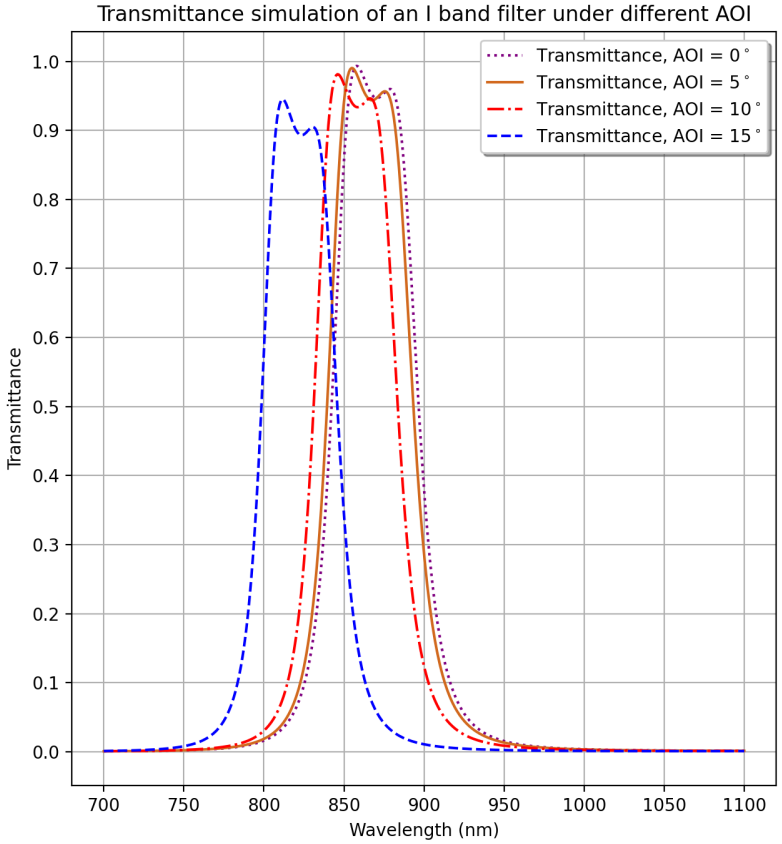

Figure 2.4: The influence of the light's angle of incidence on transmittance.

A shift of the central wavelength towards the blue region occurs. The central wavelengths now become $\lambda_0 = 862.89$ nm when $\theta = 5°$, $\lambda_0 = 859.51$ nm for $\theta = 10°$ and $\lambda_0 = 846.37$ nm at $\theta = 15°$. This is to be expected, since the central wavelength will always shift according to the relation (Löfdahl et al., 2011)

$$\lambda_\theta = \lambda_0 \sqrt{1 - \frac{\sin^2 \theta}{n^2}}. \tag{2.12}$$

By choosing some dummy values for λ_0 and n, one can show that the central wavelength value will decrease with an increasing AOI θ.

The transmittance of a filter is also influenced by the AOI. It happens due to the reduction in the optical thickness, which alters the phase difference of beams within the coating (Dobrowolski, 1978). In this example, for $\theta = 5°$, the maximum transmittance is 99%, occuring at $\lambda = 858.02$ nm, whereas for $\theta = 10°$, it slightly decreases to 98% and shifts to $\lambda = 854.71$ nm. With a more extreme angle, $\theta = 15°$, the peak transmittance is located at $\lambda = 841.78$ nm and it drops to 94%. However, AOI above 10° are of no interest for filters used in Astronomy, since they reduce transmission significantly and shift the wavelengths, which influences the performance of the instruments and the data quality.

Now that we have examined the theoretical concepts of thin film filters design, we have the necessary tools to interpret the transmission profiles of real filters. We will further look at the MICADO filters in more detail and see how their curves reflect the design principles in chapter 5.

Chapter 3

The science cases behind the MICADO filters

The development of MICADO's filters is driven by the scientific goals of the instrument. The broad-band filters I, J, H and K can be used for studying high redshifts galaxies and stellar populations in nearby galaxies. These filters enable the measurement of key physical properties, such as stellar age, metallicity and star formation rate. Besides the classical broad and intermediate band filters, a number of narrow-band continuum and specific emission line filters are included to observe at particular wavelengths that correspond to important emission lines at zero redshift, such as [FeII], Paβ and Brγ. This will enable new insights into supernova remnants, star forming regions and HII clouds within the Milky Way along with the ability to study the activity of nearby galaxies (Tolstoy & Davies, 2018). A full overview of the requirements and science cases for every MICADO filter is described in detail by Davies et al., 2022 in the *MICADO Masks, Stops, and Filters Description* document. This chapter focuses on summarizing the scientific motivation behind the selection of the three filters that are studied in this thesis:

- I-long – a broadband filter at the blue side of the MICADO wavelength coverage;
- [FeII] – a narrow-band filter designed for observing the [FeII] emission line at 1644nm;
- H-cont – a narrow-band continuum filter used to measure the continuum emission in the 1559–1582 nm wavelength window.

3.1 Studies of stellar populations: the I-long filter

The I filters, in astronomical instruments, often cover different wavelength ranges depending on instruments' sensitivity and scientific goals. The MICADO I-long filter is particularly unusual as it covers the red part of the classical I-band and the blue region of the Z-band. The lower cut-off point corresponds to the minimum sensitivity of the instrument, which is 800 nm and the upper cut-off is 934 nm to avoid the atmospheric absorption at 950 nm (Davies et al., 2022).

The main scientific driver for the I-long filter is the study of resolved stellar populations.

Deep et al., 2011 performed a case study involving the $IJHK_s$ filters on a simulated elliptical galaxy located at the same distance as the Virgo galaxy cluster, to investigate the accuracy of stellar photometry with MICADO in crowded fields and create color-magnitude diagrams. They determined that the MICADO filter combination $(I, I-K)$ yields the most detailed CMD, because the I-band expands the color range the most (see Figure 3.1). As a result, the RGB (Red Giant Branch) and the AGB (Asymptotic Giant Branch) branches are more spread out, making the interpretation of their color range more accurate. MICADO's high angular resolution and sensitivity will also make it possible to detect very faint objects, such as the brown dwarfs not only within the Milky Way, but also around its satellite dwarf galaxies (Tolstoy & Davies, 2018). Hence, MICADO will be able to expand the current catalogs of resolved stellar populations in both the local Universe and in more distant galaxies, providing deeper insights about their formation and evolution history. We will gain better understanding of the initial mass function (IMF) and how it varies across different regions within and outside our Galaxy. This information is essential for modeling galaxy evolution, as the IMF contains valuable information about the initial distribution of stellar masses, which directly influences the star formation rate, chemical enrichment and the effect of feedback processes caused by stellar evolution, stellar winds and supernovae.

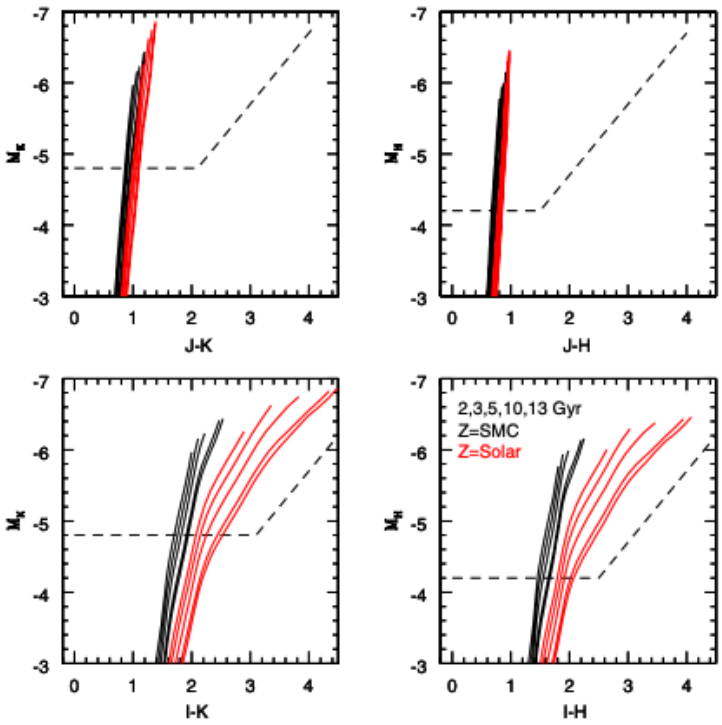

Figure 3.1: Comparison of 5 isochrones for SMC-like (Small Magellanic Cloud) metallicity, in black (from Yi et al., 2001) and solar metallicity, in red, for 5 different ages. The I-K and I-H panels show the largest spread of the isochrones, making it possible to obtain the most detailed CMDs (Deep et al., 2011).

3.2 Shock region studies: the [FeII] line

Line emission occurs when an electron transitions from a higher to a lower energy state. Due to the discrete allowed energy states, each observed emission line traces specific physical processes. Selection rules determine if an electron transition to a lower state can occur based on changes in quantum numbers that include the orbital angular momentum (ΔL), total angular momentum (ΔJ), spin (ΔS) and parity (Morrison, 2021). If at least one of these rules is violated, the transition is classified as forbidden and the probability of it happening depends on the strength of the electric quadrupole. The [FeII] emission line is a forbidden transition that occurs at 1644 nm. It is most often observed in the interstellar regions with low density, since the collisions are so rare that the involved timescales allow for forbidden radiative transitions to occur (Draine, 2011; Morrison, 2021).

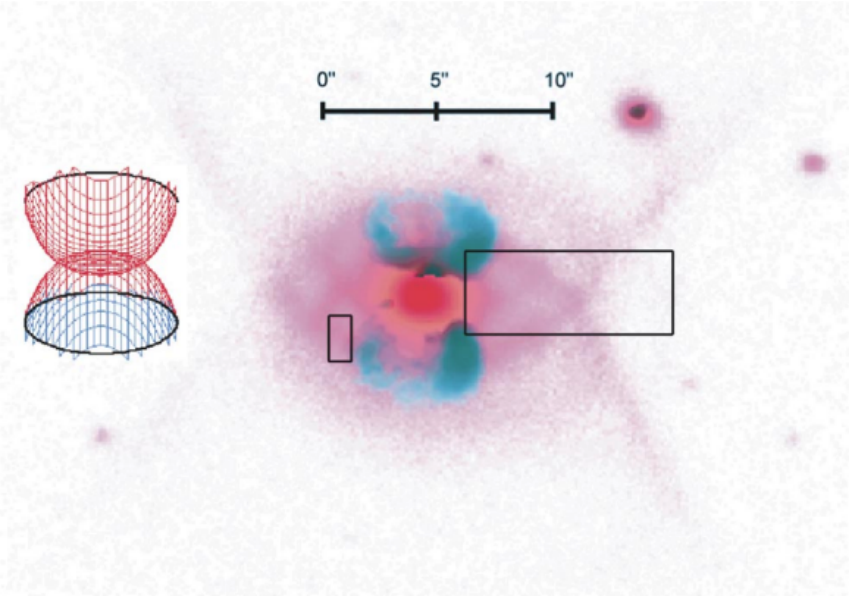

Figure 3.2: The two bubble-shaped [FeII] emission line regions observed in the Hubble 12 nebula (in blue-green). The H_2 line and the continuum emission are in red. The drawing on the left represents the geometry of the H_2 emission region, while the boxes represent the used spectroscopic slits, which are explained in more detail by Welch et al., 1999.

The [FeII] filter is a narrow band filter designed to detect the [FeII] emission line occurring at $\lambda = 1644$ nm at a redshift $z = 0$. It will be used together with the H or H-cont filters to remove the continuum in order to determine the emission-line flux. This filter is well-suited for observing shock regions within and outside the Milky Way. For example, a study of the planetary nebula Hubble 12 shows prominent lines of [FeII] in bipolar bubbles around the core (see Figure 3.2). This is caused by a fast wind originating from the central star (Welch et al., 1999). The bubbles may indicate either an inner shock from a fast wind, a second wind that occurred at a later stage or that the [FeII] emission line is caused by cooling of a photodissociation or HII region. Shock regions can also be found in starburst regions, as it is the case for the young stellar object (YSO) Gaia19bey around which an [FeII] emission region in the shape of an edge-on disk was discovered (Hodapp et al., 2020).

By employing MICADO's capabilities, more planetary nebulae and YSOs can be studied in detail with high spatial resolution, looking for traces of [FeII] to gain insights on the formation and evolution of shock regions and their cooling mechanisms, which will deepen our understanding of astrophysical magneto-hydrodynamics.

3.3 Solar system observations: the H-continuum filter

Continuum filters play a crucial role when observing with narrow-band filters, making it possible to separate an emission line flux from the continuum flux in order to study the physical properties of the emission line (e.g. di Serego Alighieri, 1987). The MICADO H-continuum filter will serve as an off-band continuum pass for the [FeII] narrow band. It will also be used for observations within the solar system to investigate the deep continuum of the planetary atmospheres and the ice present in various nearby astronomical objects (Davies et al., 2022).

An important research question today is what is the distribution and state of water found outside Earth. MICADO's high spatial resolution and sensitivity will enable accurate spectra of small and faint objects to study the processes that influence the composition of water ice. This can provide valuable information about the properties of the Trans-Neptunian Objects (TNOs), which are typically too faint to study with current facilities. This will offer new insights on the overall formation and evolutionary history of our solar system.

In addition, the gas giants Uranus and Neptune must have formed in a low density region of the proto-planetary disk, so, their rock and ice accretion processes around the central cores occurred slower than for the other giants. Even though the two planets share a similar atmospheric composition and temperature, they are very different from each other in many aspects. Hence, it is important to understand their vertical atmospheric composition and the H-continuum filter, together with other filters (e.g. K-mid, K-short), will provide valuable data by allowing detailed observations of the different layers.

Besides the gas giants themselves, their satellite moons offer further opportunities to investigate the distribution of water ice. For instance, Jupiter's moon, Europa, is believed to host an ocean under a thick ice layer, which could be a valuable exobiological research target. Similarly, Neptune's satellite, Triton, with its rich atmosphere and icy surface, could provide valuable information about the processes of water enrichment and the evolution of icy bodies. By employing MICADO's sensitivity and high spatial resolution, the H-continuum filter in combination with other filters, such as, for example, K-short, K-mid and J, will enable studies that will refine our current understanding about the formation and evolution of the solar system (Tolstoy & Davies, 2018).

Chapter 4

The experimental setup

The MICADO optics need to operate at cryogenic temperatures. Hence, the filters need to satisfy a series of requirements, which include maintaining the transmittance performance at 82 K, while withstanding the cooling and heating cycles. In order to asses these properties, we performed measurements of the transmission spectra of the I-long, [FeII] and H-cont witness samples at temperatures of 82 K, 100 K and 293 K. We used the equipment available in NOVA's optical lab, which will be described briefly in this section.

4.1 Overview of the spectrometer

To measure the transmittance of the witness samples, we used a Varian FT7000e Fourier Transform Spectrometer (FTS) in the optical lab of NOVA. The instrument is equipped with both near-infrared (NIR) and mid-infrared (MIR) internal Helium light sources, but external sources can be connected if needed. Some optical elements in the spectrometer can be exchanged to modify the beam shape before the measurement compartment. These elements include a beam collimator, a flat folding mirror and a parabolic mirror. The latter is used to focus the light coming from the source such that it passes through the middle of the sample placed in the sample compartment. In addition, the spectrometer is equipped with a system that maintains a continuous flow of dry air to prevent any moisture buildup that could introduce absorption lines in the measured spectra (van den Born et al., 2024).

By selecting appropriate configurations, which include the light source, the beam splitter and the detector, it is possible to obtain spectra starting from 250 nm in the ultraviolet, up to 67 µm in mid-infrared. The available configurations of this spectrometer are UV-VIS, VIS, NIR1, NIR2, MIR1, MIR2 and they are selected according to the wavelength range of interest using an application connected to the device. In this test campaign, we took measurements with the NIR1 setting for the I-long witness samples and NIR2 for the [FeII] and H-cont witness samples, which required to change the detector. A detailed overview of the difference in parameters between the two modes is given in Table 4.1.

Table 4.1: Spectrometer configurations for measurements in NIR1 and NIR2. Note that these 2 settings require different detectors, optical filters, and aperture sizes, while all the other parameter settings remain the same.

Parameters	**Settings tab**	**NIR1**	**NIR2**
λ (nm)		500–1163	1000–3571
Wavenumber (cm^{-1})		20000–8600	10000–2800
Speed (kHz)	Electronics	5	5
Filter (kHz)		5	5
UDR		0.5	0.5
Resolution (cm^{-1})		2	2
Sensitivity		1	1
Scans to Co-add		128	128
IR-source	Optics	NIR (S-W halogen)	NIR (S-W halogen)
Beam		Internal	Internal
Detector		Si	DTGS
Beam splitter		NIR-Quartz	NIR-Quartz
ATR crystal		None	None
Optical filter		8 mesh grids	None
Aperture		2	0.25
Interferometric Symmetry	Advanced	Symmetric	Symmetric
Gain Ranging		Enabled	Enabled
Gain Ranging radius		40	40
Background scans to co-add	Background	128	128

Based on the experience gained by myself and my colleagues from NOVA, the stability of the light source can influence the measured transmission levels up to a few percent. In addition, the varying humidity and temperature in the optical lab has an effect on the resulting transmission curves by introducing unwanted absorption lines. These issues can be mitigated by allowing sufficient time for the light source to warm up and by waiting at least 15 minutes after opening the sample compartment to ensure that it is properly flushed with dry air. In order to get an overview of the light source's stability, it is recommended to take a background measurement between each sample measurement to check for any deviations in the response curves.

4.2 Cryogenic environment control using CRiSP

To perform measurements of the transmission of the witness samples in a cryogenic medium, NOVA developed and assembled a cryostat that can fit in the sample compartment of the Varian FT7000e FTS, hence the name CRyostat in SPectrometer or CRiSP (see Figures 4.1 and 4.2). Its exterior is made from aluminum and the door used to access the filter wheel features a copper ring that ensures vacuum sealing. To maintain thermal stability, the filter wheel is enclosed in a copper housing covered by multi-layer insulation (MLI), as seen in Figure 4.5.

The wheel can accommodate up to six samples of 25 mm in diameter, while at least one slot must stay empty to allow for background measurements. A stepper motor, fixed on top of the cryostat, is connected to the motor axis. The latter moves the worm wheel, that, in turn, rotates the sample wheel. The sample wheel can rotate both clockwise and anti-clockwise. A series of notches on the sample wheel ensure that it is locked in a stable position for taking measurements (see Figure 4.3). In order to move from one slot of the wheel to the next, the external stepper motor has to rotate by 6084°. This motion is controlled with the application OWISoft installed on a laptop in the Optics lab of NOVA. Temperature sensors are attached on the cold head of the cryocooler, on the thermal shield, on the sample wheel and on a dummy mass. A CryoCon temperature controller adjusts the temperature via a Proportional-Integral-Derivative (PID) closed-loop, which receives real-time feedback from the sensor attached to the cold head.

Before reaching the sample inside CRiSP, the light passes through a long and narrow tunnel that reduces the stray light and the thermal radiation from the warm external environment. CRiSP features two such tubes (see Figure 4.4). One of them has a Cadmium Telluride (CdTe) window, which is used when taking measurements in mid-infrared. Its transmission varies between 60 and 70% within the 1.5 to 2.8 µm wavelength range. The other tunnel features a Sapphire window that allows for transmission above 80% between 0.2 and 4 µm, covering the UV, visible and IR regions (van den Born et al., 2024).

During this testing process, the witness samples are carefully handled in a laminar flow cabinet to avoid dust deposits. However, they still need to be integrated in the cryostat quickly to avoid contamination. One has to make sure that each sample is secured in one of the 6 available slots using customized springs and a ring. For accurate tracking of the sample wheel's position, each slot is numbered, as seen in Figure 4.3. Since CRiSP matches the dimensions of the sample compartment of the FTS and maintains a vacuum during operations, deep absorption lines from the ambient humidity should not be observed.

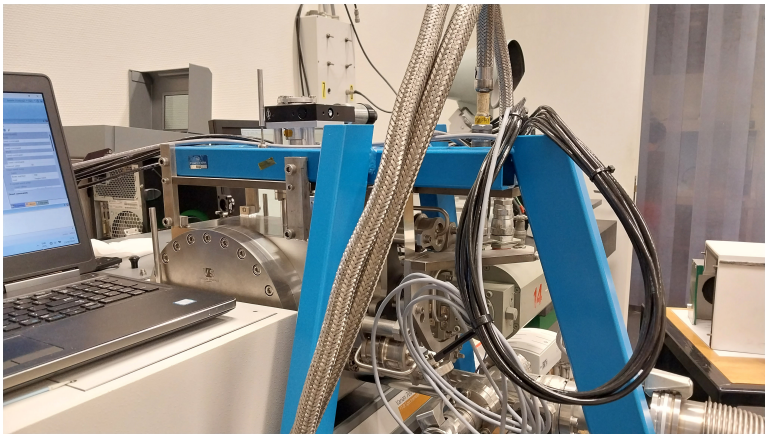

Figure 4.1: The final setup showing CRiSP integrated in the sample compartment of the Varian FT7000e FTS, while connected to the Helium cooling source and to the vacuum pump.

Figure 4.2: CRiSP viewed from the outside. The stepper motor is located on the top, while on the right, the mechanisms used to connect and control the vacuum pump and liquid helium source are visible.

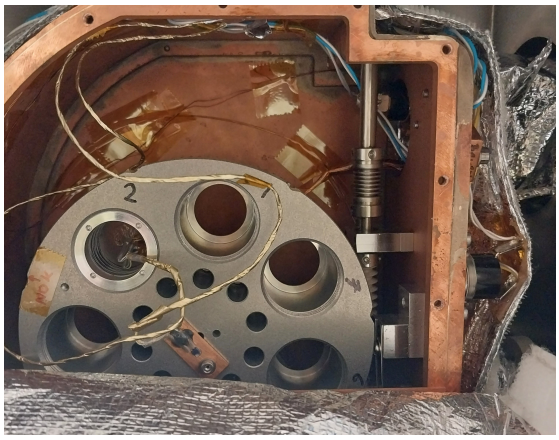

Figure 4.3: The sample wheel with thermal sensors attached to it. The rotation mechanism, that includes the worm wheel, is located in the back right of the copper housing. The small dips in the wheel are the notches that secure the wheel's position when taking measurements.

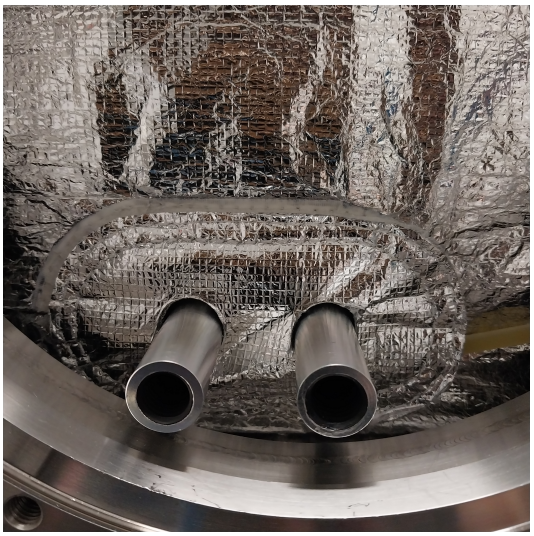

Figure 4.4: The tunnels through which the spectrometer light passes. The one on the right was used in this test campaign and it features a Sapphire window. The one on the left has a CdTe window.

Figure 4.5: The copper housing and the MLI cover that enclose the sample wheel in order to ensure thermal control.

Chapter 5

Results and analysis

Two companies are responsible for coating MICADO's optical filters based on the requirements defined by NOVA. The narrow band filters are coated by the French company Cilas, while the broad bands – by SCHOTT in Switzerland. We received two I-long, two [FeII] and two H-cont filters and two corresponding witness samples for each of them. Only one filter from each pair will be placed in the filter wheel or in the pupil wheel of MICADO, while the other will serve as a spare.

As soon as the filters arrived, we inspected them by eye and using a microscope in the laminar flow cabinet in the clean room of NOVA. Afterwards, we integrated the witness samples in CRiSP and measured their transmission. The obtained results were compared with the documented requirements and with the data provided by SCHOTT and Cilas. To reach a final conclusion whether the filters will be accepted and used in MICADO, a wavefront error (WFE) measurement test has to be performed in order to identify if there are any optical aberrations that could lead to the degradation of the image quality (Argueta, 2025). This test will be performed by other colleagues from NOVA.

5.1 Methods

The first part of the MICADO filters' testing campaign took place between the 21st May and the 23rd June 2025. A visual inspection of all the filters was conducted to check for the quality of the coating and defects. This is an important step, since it allows for tracing any new imperfections that can occur in the event of cryogenic environment failure or accidental surface damage. A delay in the delivery of the I-long filters and witness samples, along with a failure of one of CRiSP's components (described in the Appendix), affected the schedule of the test campaign. Thus, the witness samples were integrated in the cryostat on the 13th of June and the transmission data was collected between the 16th June and the 23rd June. After placing each witness sample in one of the slots, the home position of the wheel was defined in the OWISoft application as the empty slot 2 in front of the Sapphire tunnel. This allows for easy tracking of the samples inside the closed cryostat. Slot 5 was also left empty for taking background measurements, while the dummy mass with a thermal sensor was placed in slot 7. An overview of the witness samples used in this test campaign and

their location in the CRiSP's sample wheel is given in Table 5.1. Note that due to the small number of slots in CRiSP, only one [FeII] sample and one H-continuum sample were tested.

The transmission measurement of every witness sample was carried out according to the following procedure:

1. A background measurement was taken at an open slot (2 or 5) next to the witness samples that were measured.
2. The sample wheel was moved to the position where the spectroscope's light passed through the sample to be tested.
3. A measurement of the sample was taken.
4. The sample wheel was moved to the position of the other filter that used the same spectrometer settings.
5. A measurement of the second witness sample was taken.
6. The wheel was moved to home position (slot 2).
7. The spectrometer's settings were changed from NIR2 to NIR1 or vice-versa and the steps 1-6 were repeated.

This process was done at the temperatures of 293 K, 101 K and 84 K. However, in the further analysis, we will omit the measurements taken at 101 K, because this is an intermediate temperature at which the filters will most likely operate for the first time, when MICADO will be commissioned. However, taking measurements at an intermediate temperature is important, since it simulates a cryogenic cycle, allowing us to verify if the samples remain undamaged under temperature changes.

Since the [FeII] and H-continuum filters required a different spectrometer configuration than the I-long filter, it was necessary to add mesh grids in front of the latter, as indicated in Table 4.1. Without them, the spectrometer's application would show an error because of a signal overflow. Hence, we had to remove a cover of the spectrometer, as depicted in Figure 5.1 in order to make space for placing the mesh grids. This introduced absorption lines in the background taken with the NIR2 setting at the temperature of 100 K, since the insides of the spectrometer were not flushed with dry air and the DTGS (Deuterated Tri Glycine Sulfate) detector is particularly more sensitive (see Figure 7.1 in the Appendix). Since we were aware of this issue, it was decided to begin by measuring only the [FeII] and H-cont transmissions at 293 K and 84 K, which ensured that the spectrometer was properly flushed with dry air. Only after these two measurements were taken, the spectrometer's cover was removed and the first measurements of the I-long filter were taken. After finishing taking the transmission measurements, the witness samples were carefully taken out of the cryostat, inspected and stored back in the boxes containing the filters.

Table 5.1: The witness samples used in the test campaign and their location in the sample wheel

Witness sample	Serial number	Slot in the sample wheel
[FeII]	252B101, 252 B140/142, FeII 132a	1
H-cont	252B121, 252 B140/142, 211a	3
I-long	M	4
I-long	C	6

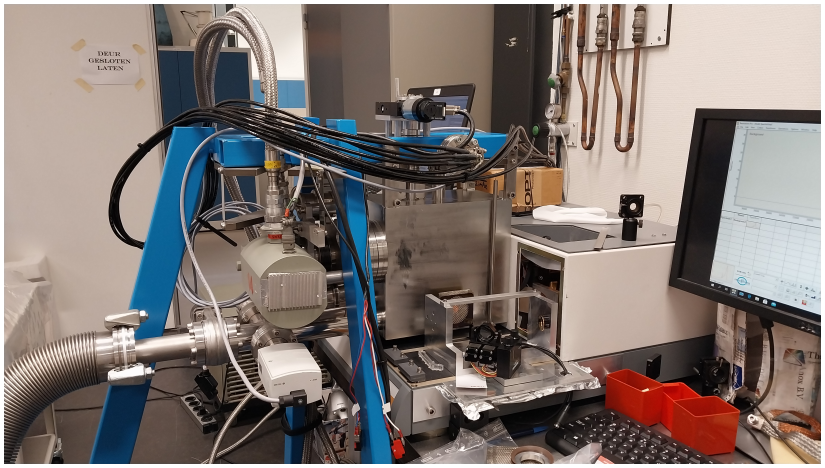

Figure 5.1: CRiSP seen from the back. On the right, the spectrometer's cover was removed in order to place mesh grids in front of the Sapphire window through which the light beam passes before reaching the filters.

5.2 General filter specifications

The broad- and intermediate band filters will be placed in one of the two filter wheels at a tilt of 3.75° to avoid ghosting effects, which are caused by the light being reflected repeatedly within the system. The narrow band filters will be mounted in a flat position in the pupil wheel, because a tilt would result in a 30% shift of the full wavelength range. All filters have a well specified region where transmission (T) must be at least 50%. Within this region, the averaged peak transmission (APT) range is defined and it is the range in which a filter's transmission must be above 90%. However, it is also important to attain the blocking requirement in order to prevent light from outside the transmission window from reaching the detector. The blocking is set by defining accurately the cut-on and the cut-off wavelengths, which represent the beginning and the end of a bandpass. All filters must match the required transmission spectra at 82 K – the temperature at which they will operate and shall have a maximum ringing of 2% (Davies et al., 2022, Janssen et al., 2024). The latter is defined as the deviation from the weighted average of the transmission above 90%. Last, the measured CWL should deviate from the theoretical CWL by less than 0.3% for the narrow-band filters and less than 0.5% for the broad-band filters. An overview of the wavelength window requirements for the filters and their corresponding witness samples is given in Table 5.2.

Table 5.2: The wavelength specifications of the 3 filters used in the test campaign. Adapted from Davies et al., 2022 and Janssen et al., 2024.

Filter	$\lambda_{central}$ (nm)	λ_{cut-on} (nm)	$\lambda_{cut-off}$ (nm)	**T > 50%** (nm)	**Avg. peak T** (nm)	**Notes**
I-long	867.0	800.0	934.0	800.0 – 934.0	804.3 – 929.7	
[FeII]	1649.5	1638.5	1660.4	1638.5 – 1660.4	1642.6 – 1656.3	Line (z=0) at 1644.0 nm
H-cont	1570.0	1558.5	1581.5	1558.5 – 1581.5	1562.4 – 1577.6	

5.3 The [FeII] filter

Two [FeII] filters, accompanied by two witness samples were coated by the French company Cilas. They have a diameter of 100 mm and are 8 mm thick. The substrate used for the [FeII] filters is Infrasil 302, which is a type of optical quartz that is often used for IR filters (UQG Optics Ltd., n.d.). The accompanying witness samples measure 25 mm in diameter and 2 mm in thickness. The coating was deposited on a Corning 7980 substrate, which is a type of pure non-crystaline fused silica glass (Corning, 2015) and it is almost identical to infrasil.

5.3.1 Visual inspection of the [FeII] filters

The two [FeII] filters can be distinguished by their serial numbers SN31 (see Figure 5.2) and SN32. On face 2 of the SN31 filter, we found an inclusion measuring approximately 0.5 mm in length in the coating and it was also reported by Cilas as L0.016 (see Figure 5.3), which is an optics notation used to indicate the area of a defect. It has an elongated shape and creates the effect of bending light around it, which leads to a colorful pattern, as seen in Figure 5.4. A scratch measuring 1 mm has also been noticed and was traced back as L0.010 in the Cilas' report (see Figures 5.3 and 5.5). These imperfections are not considered a threat to the filter's performance due to their small size.

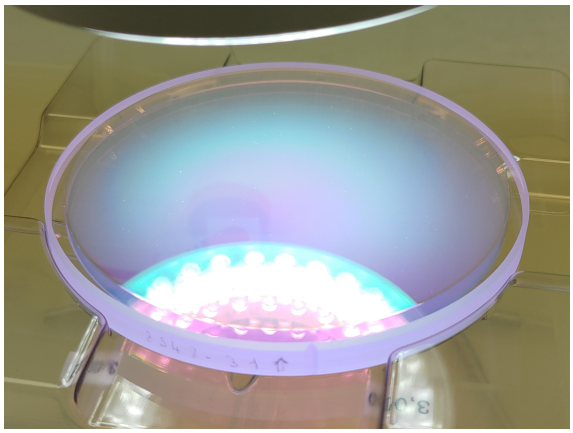

Figure 5.2: The 100 mm [FeII] filter with serial number SN31 under the microscope's light.

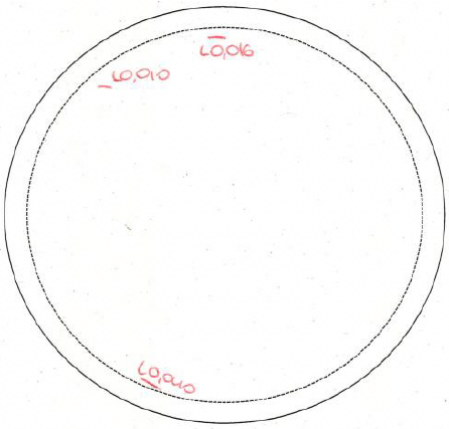

Figure 5.3: The defects map provided by Cilas for face 2 of the [FeII] filter with the serial number SN31. The numbers in the notation indicate the area of a defect.

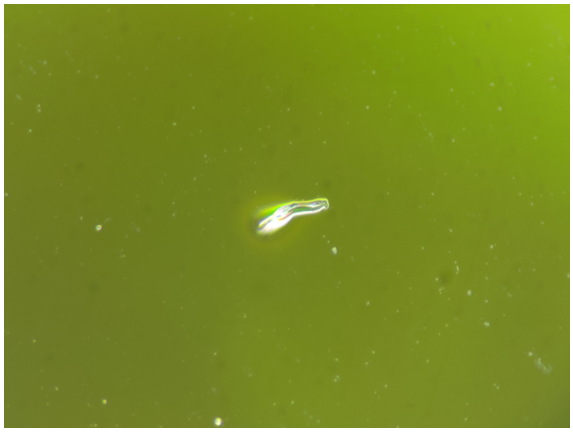

Figure 5.4: Defect with the size of 0.5 mm in length that creates a colorful pattern in the coating of the [FeII] filter with serial number SN31. Marked by Cilas as L0.016 in Figure 5.3.

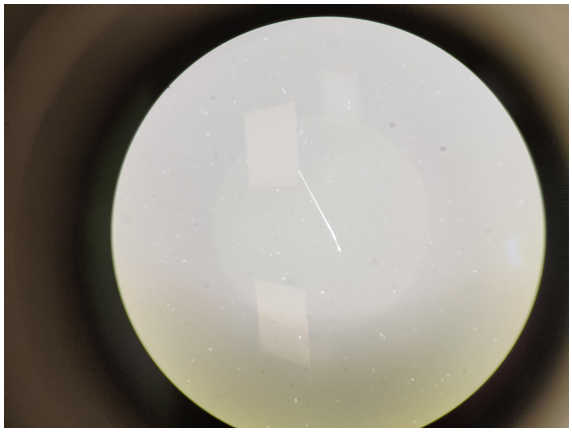

Figure 5.5: Scratch with a length of 1 mm on the surface of the [FeII] SN31 filter seen through the microscope at maximum zoom. Marked by Cilas as L0.010 in Figure 5.3.

Some damage with an irregular shape at the edge of the coating represents the largest defect on face 2 of the [FeII] SN31 filter and it is depicted in Figure 5.6. It is mentioned by Cilas as L0.040 in Figure 5.3. These types of defects can occur during the coating process, but the companies should strive to minimize them. Since this imperfection is outside the clear aperture, it will not affect the performance of the filter.

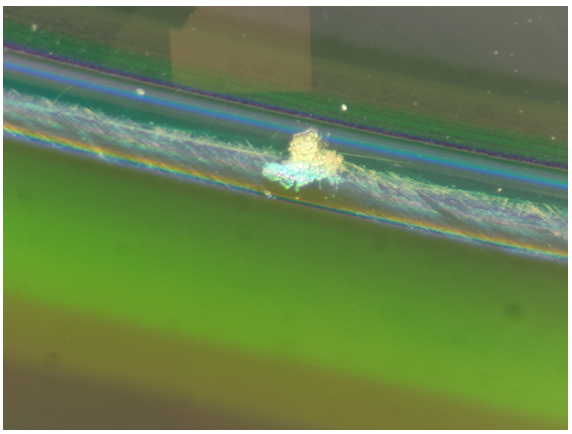

Figure 5.6: Defect with an irregular shape at the edge of the coating of the [FeII] SN31 filter, measuring approximately 1 mm in length and 1 mm in height. Marked by Cilas as L0.040 in Figure 5.3.

Cilas did not report any defects for the [FeII] SN32 filter and during the inspection performed at NOVA, we did not notice anything concerning on the filter's surface. Yet, under good light and with a microscope, we observed some dots and deposits of dust on both surfaces of the SN31 and SN32 filters, but the latter are usually easy to remove with a special cloth. Some of the dots were clustered very closely together in multiple regions and two examples are shown in Figures 5.7 and 5.8. The reason behind their occurrence has not been identified yet, but

Cilas is currently investigating the potential causes. No such defects have been noticed on the witness samples. To asses the influence of these dots on the performance of the filters, a wavefront error (WFE) measurement test has to be performed, but it is outside the scope of this thesis.

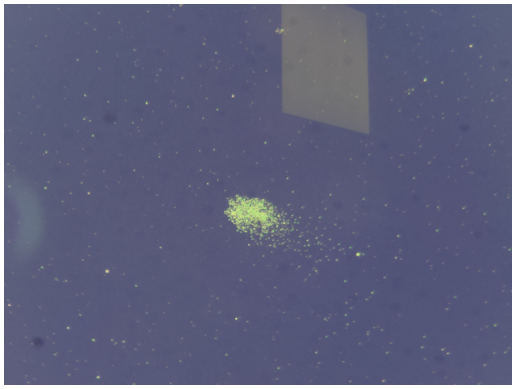

Figure 5.7: Region of clustered polishing dots on the [FeII] SN31 filter.

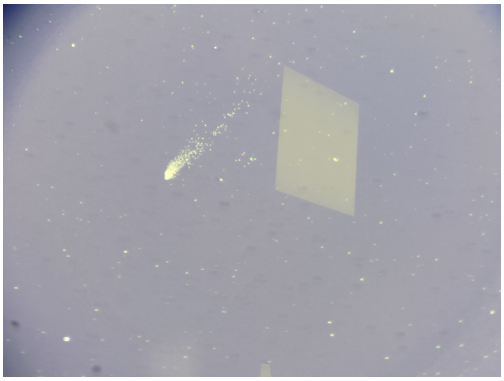

Figure 5.8: Region of clustered polishing dots on the [FeII] SN32 filter.

5.3.2 Transmittance of the [FeII] filters

To evaluate how the [FeII] filters' transmittance varies with temperature, the transmittance of one witness sample was measured at 293 K, 100 K and 84 K. As seen in Figure 5.9, the overall shape of the transmission profile is unchanged, but a clear shift of the bandpass region towards blue wavelengths is observed at lower temperatures. At 84 K, we found that the transmittance is 2.78% lower than at 293 K. This decrease can be attributed to the fluctuating stability of the light source and the temperature dependence of the coating's refractive index, but the latter is not properly understood yet (Hecht, 2017).

To calculate the spectral shift, the measurement taken at room temperature is used as the reference and it is denoted by T_{ref}. A subsequent measurement, T_i, is then shifted along the wavelength axis by an amount $\Delta\lambda$, to determine a point at which the difference between the two transmission curves is minimized. This difference is quantified through a root sum square (rss) of the difference between the two transmission curves. To find the wavelength shift $\Delta\lambda_T$ that minimizes the rss difference, a scalar minimization function is used. A mathematical description of this method is given by

$$\Delta\lambda_T = \min_{\Delta\lambda} \sqrt{\int_{\lambda_1}^{\lambda_2} [T_{\text{ref}}(\lambda) - T_i(\lambda + \Delta\lambda)]^2 d\lambda}, \qquad \text{with } w_1 \leq \Delta\lambda \leq w_2. \tag{5.1}$$

In the above equation, λ_1 and λ_2 are the boundaries of the region where the spectral shift occurs and w_1 and w_2 define the optimization window and are set equal to the wavelength boundaries (van den Born et al., 2024). Choosing $\lambda_1 = 1620$ nm and $\lambda_2 = 1685$ nm, it was determined that the spectral shift of the [FeII] witness samples is 2.01 nm. To check the accuracy of this result, a shifted reference curve was placed on top of the measured transmission at 84 K, as depicted in Figure 5.10.

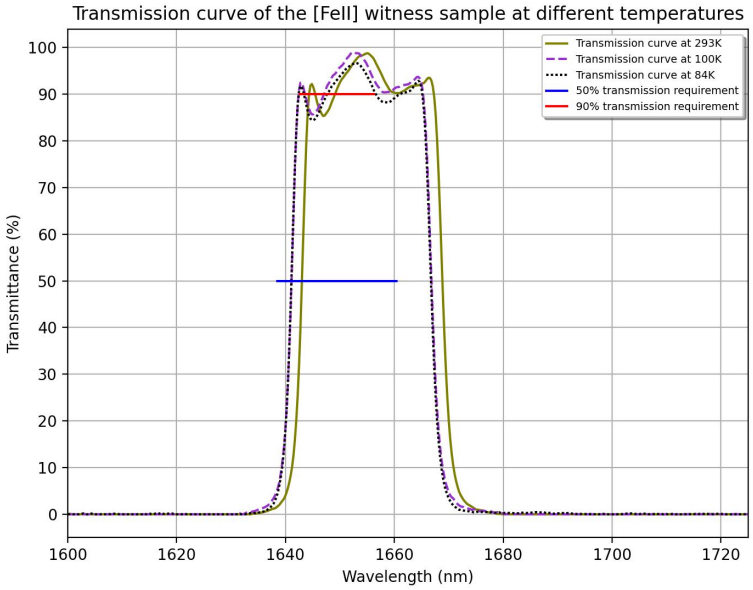

Figure 5.9: Comparison of the transmission spectra of the [FeII] witness sample at 293 K, 100 K and 84 K. The red and blue horizontal lines indicate the regions where the transmission has to be larger than 90% and 50% respectively.

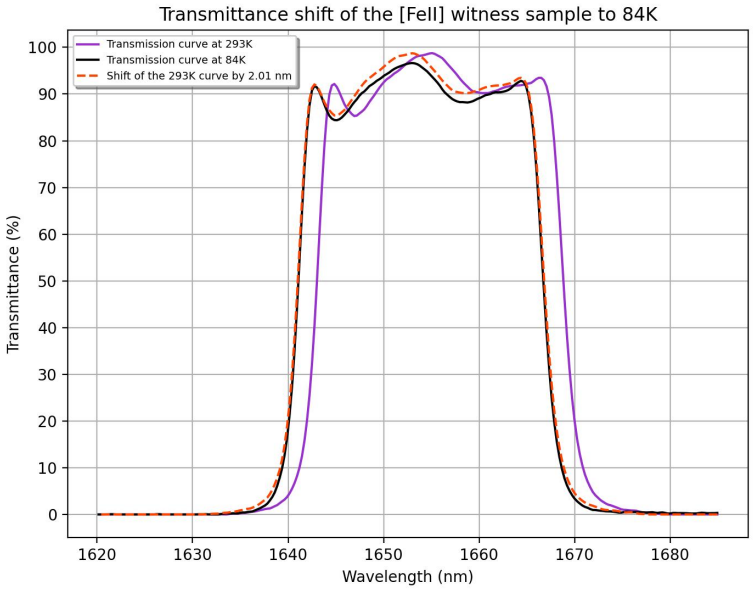

Figure 5.10: The reference transmission curve of the [FeII] witness sample measured at 293 K (in purple) was shifted on top of the measured transmission spectrum at 84 K. The shift was obtained by minimizing the root sum squared difference between the 2 measured spectra, obtaining a shift of 2.01 nm.

Having collected the data, it is now possible to quantify whether the witness sample and the two [FeII] filters meet the specified requirements for the central wavelength (CWL), the shift of the measured CWL from the theoretical CWL and ringing. The results are focused on the transmission obtained at the temperature 84 K as it corresponds to the operational temperature of MICADO. Since the transmission regions of the two filters and the witness sample do not have a symmetric shape, especially around the top, the weighted average of the data points was used throughout the data analysis process. To compute the ringing, the transmission data points above 80% were selected to include the dips. Then, the weighted average of the transmission was calculated as

$$\langle T \rangle = \frac{\sum_{i=1}^{n} \lambda_i \cdot T_i}{\sum_{i=1}^{n} \lambda_i}, \tag{5.2}$$

where λ_i stands for the ith wavelength and T_i is the corresponding transmittance value. Next, the weighted mean of the squared transmission data points, $\langle T^2 \rangle$, was obtained via the relation

$$\langle T^2 \rangle = \frac{\sum_{i=1}^{n} \lambda_i \cdot T_i^2}{\sum_{i=1}^{n} \lambda_i}, \tag{5.3}$$

where the symbols keep their previous meaning. Using the above quantities, the variance is computed as

$$\text{var} = \sigma^2 = \langle T^2 \rangle - \langle T \rangle^2. \tag{5.4}$$

Finally, by taking the square root of the variance, we obtain the deviation σ, which quantifies the average distance of the transmission data points from $\langle T \rangle$. This deviation represents a measure of the sample's ringing and the obtained value is included in Table 5.3.

The central wavelengths of the [FeII] filter and witness sample were computed using the transmission weighted average of the wavelength given by Equation (2.11) from chapter 2 and the results are presented in Table 5.3. The CWL will further be used to determine whether the filters and the sample meet the required limit for the CWL deviation. This is done fairly simply by first computing 0.3% from the theoretical CWL of the filter, $\lambda_0 = 1649.5$ nm. Afterwards, the obtained value was compared to the difference between the theoretical CWL and the CWL at 84 K. If the difference falls within the 0.3% , then the filter is considered compliant.

We were able to directly measure the CWL of the witness sample at each temperature. However, because NOVA doesn't have a setup that could be used to quantify the transmittance of the filters, we had to use the transmittance measurements made by Cilas at room temperature. In order to get an approximation of how the transmission window would look for the [FeII] SN31 and [FeII] SN32 filters at 84 K, we subtracted the sample's thermal shift of 2.01 nm from Cilas' data. The same statistics was applied on the newly obtained transmission curves of the two filters in order to obtain their CWL at 84 K.

Since the spectrometer performs internal calibrations within the system, it can be assumed that the errors in the wavelength measurements are negligible. However, by comparing the measured HeNe laser emission line present in the background measurement at $\lambda = 632.87$ nm,

to its true value of 632.8 nm (Paschotta, 2019), an uncertainty of 0.07 nm can be assigned to all the wavelength measurements from this test campaign.

Table 5.3: Summary of the measured parameters for the [FeII] filter requirements.

Filter	Theoretical CWL	CWL at 293K	CWL at 84K	Shift from theoretical CWL	Maximum allowed shift	Ringing	Compliance
[FeII] sample	1649.5 nm	1655.92 nm	1653.94 nm	4.44 nm	4.95 nm	3.40%	Yes
[FeII] SN31		1654.00 nm	1651.99 nm	2.49 nm		2.48%	Yes
[FeII] SN32		1655.40 nm	1653.39 nm	3.89 nm		2.45%	Yes

We determined that the measured CWL at 84 K falls within the 0.3% of the theoretical CWL for both filters and for the tested witness sample. We found that the ringing of the witness sample is larger than the ringing of the filters. This can be explained by the presence of a larger dip at around 1645 nm in the transmission curve of the sample, which increases the variation in the transmittance above 80%. The ringing values for the filters are also larger than the requirement of 2%, because this requirement was not included in the working statement sent to the companies. However, the difference between the theoretical and calculated ringing values is too small and can be considered negligible.

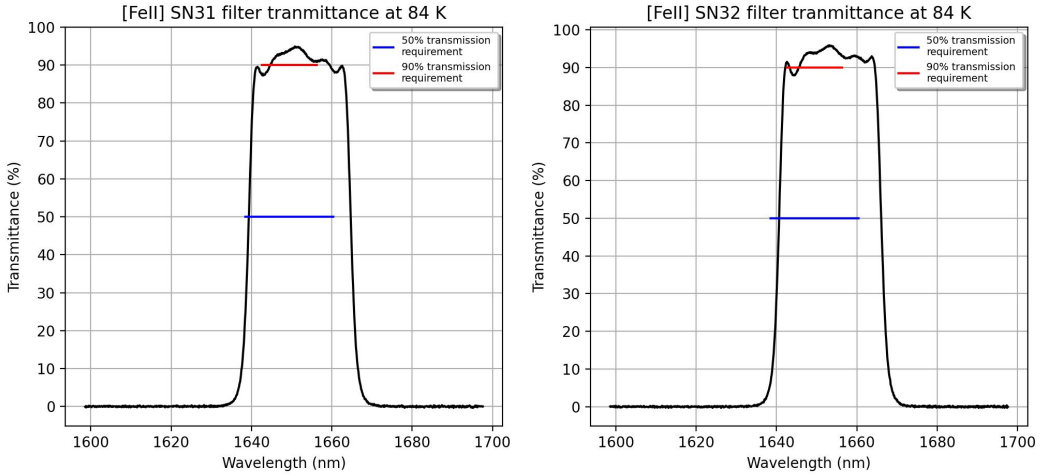

Figure 5.11: The transmission curves of the two [FeII] filters after applying a blue shift of 2.01 nm to their wavelength values. This is an approximation of how the bandpass region would look at a temperature of 84 K. The original data was provided by Cilas and it was collected at room temperature.

As mentioned previously, to predict how the [FeII] SN31 and [FeII] SN32 filters transmission windows will behave at a temperature of 84 K, we subtracted the sample's thermal shift of 2.01 nm from the wavelength data provided by Cilas, leaving the transmittance intact. The resulting shifted curves are shown in Figure 5.11. The dip around 1643 nm is less prominent than the one in the witness sample and the transmission peak in the red region of the bandpass is flatter, especially in the SN32 filter. Even if the 50% and 90% transmission requirements are slightly outside the transmission region, the deviation of the computed CWL

from the theoretical value dictates the compliance of the filter (see Table 5.3). Hence, the [FeII] filters meet the transmission requirements and will be accepted if the WFE measurements yield satisfying results.

After taking the witness sample out of CRiSP, it was visually inspected in the laminar flow cabinet. No new defects were noticed on its surface, confirming that the coating and the substrate withstanded the cryogenic cycle.

5.3.3 Observation limits with the [FeII] filter

In order to visualize the [FeII] line at 1644 nm, we plotted it alongside the transmission curve of the SN31 filter at 84 K (see Figure 5.12).

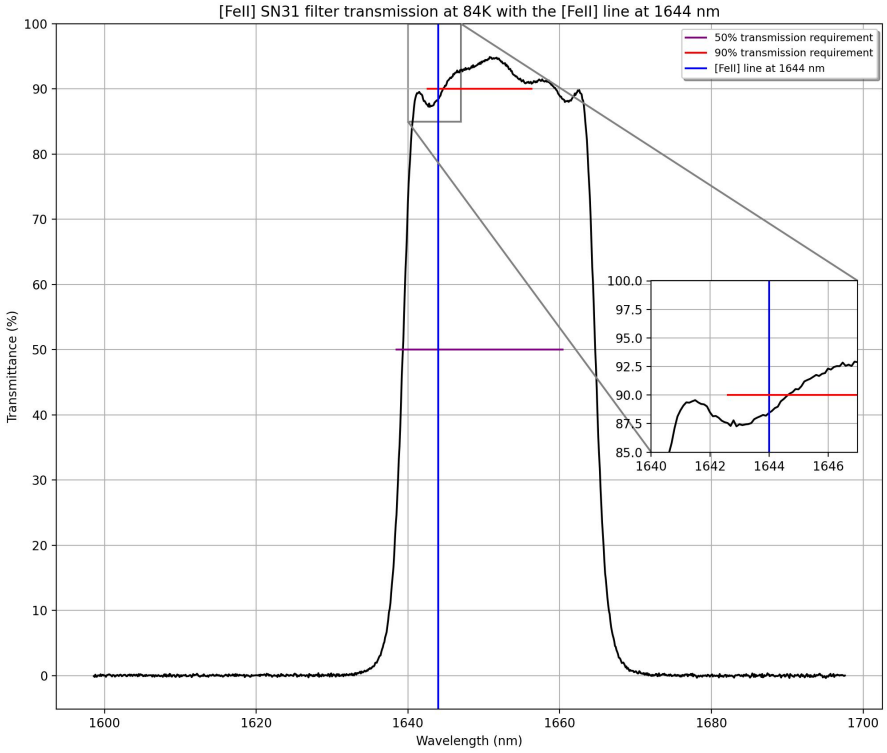

Figure 5.12: The location [FeII] line at 1644 nm (blue) within the measured transmission window of the [FeII] SN31 filter at a temperature of 84 K.

The [FeII] emission line is positioned at the blue end of the transmission region of the filter, allowing for observations at redshifted velocities. The 50% cut-on and cut-off points of the transmission curve define the minimum and the maximum wavelengths that can be observed with the [FeII] filter. The smallest observable wavelength is $\lambda_o = 1639.32$ nm, yielding a velocity of –856 km/s, where the minus sign indicates that the objects are moving towards

us. At the other end of the transmission range, a source emitting at an observable wavelength $\lambda_o = 1664.69$ nm, corresponds to a velocity of 3784 km/s for the objects moving towards us. These velocities make it possible to detect, for example, emissions from planetary nebulae that expand with velocities of approximately 42 km/s (Jacob et al., 2013), and from galaxies, such as those in the Fornax cluster, which move away from us at varying velocities of up to 1800 km/s (Chaturvedi et al., 2021).

5.4 The H-continuum filter

The two H-continuum filters and their witness samples were coated by Cilas and have the same physical properties as the [FeII] filters. Their diameter is 100 mm and they have a thickness of 8 mm. The substrate used for the H-continuum filters is Infrasil 302. The witness samples measure 25 mm in diameter and are 2 mm thick. Their coating was deposited on a Corning 7980 substrate.

5.4.1 Visual inspection of the H-continuum filters

The H-continuum filters have the serial numbers SN10 and SN18. Cilas did not report any defects on the surfaces of the two filters. Yet, during the visual inspection we found a series of imperfections using the microscope. At the edge of the H-continuum SN18 filter, 4 scratches spanning over 2 mm were observed. Their location and aspect are shown in Figures 5.13 and 5.14. They are far enough from the clear aperture not to influence the performance of the filter, but by carrying out a wavefront error (WFE) test, more insightful conclusions on this aspect can be obtained.

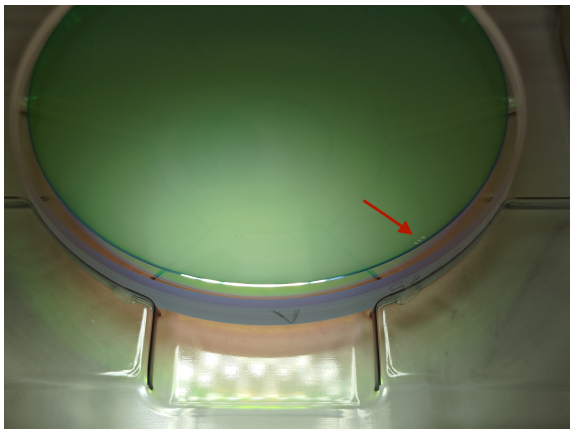

Figure 5.13: The 100 mm H-continuum SN18 filter with damage at the coating's edge, located in the lower right region as indicated by the red arrow. The defect can be distinguished by its white color.

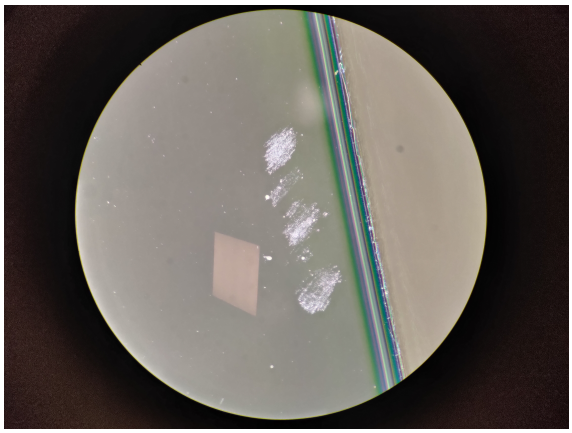

Figure 5.14: The damage at the coating edge of the H-continuum SN18 filter seen through the microscope at maximum zoom. It spans over a distance of approximately 2 mm.

In the H-continuum SN10 filter, 3 defects situated close to each other were discovered and are marked by numbers and red arrows in Figure 5.15. The first one has a tilted U shape and measures approximately 0.5 mm in length. The second imperfection is a straight line, while the third is shaped like letter J and both extend for approximately 1 mm. Zoomed-in pictures of the 3 defects are presented in Figures 5.16 and 5.17. Since their sizes are small, they will not impact the filter's performance.

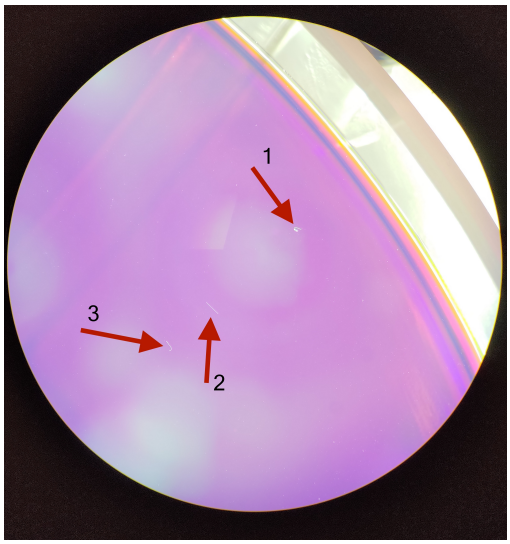

Figure 5.15: 3 defects on the H-continuum SN10 filter, indicated by red arrows and numbered for easy reference.

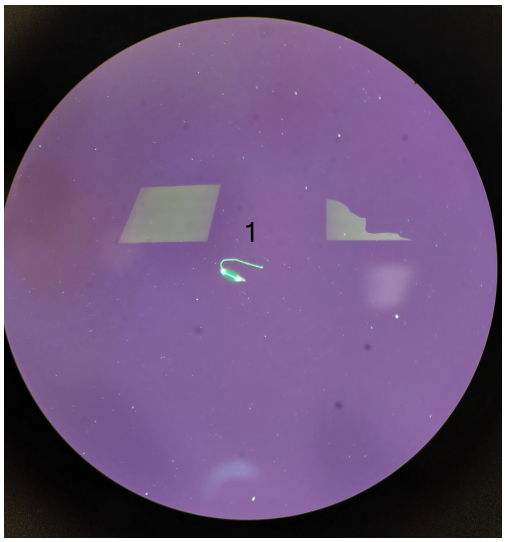

Figure 5.16: Zoomed-in picture of the first defect, measuring 0.5 mm in length, from the H-continuum SN10 filter.

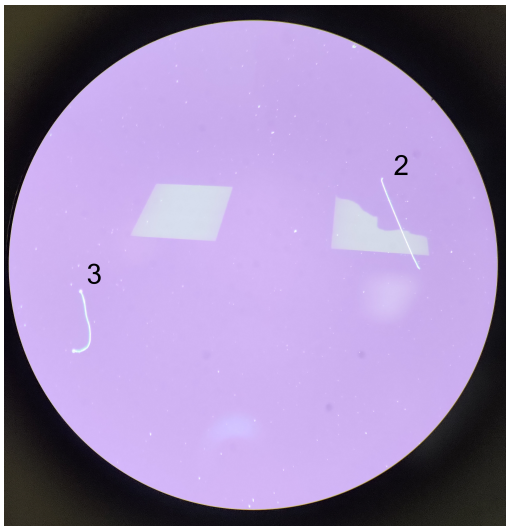

Figure 5.17: Zoomed-in picture of the defects 2 and 3 from the H-continuum SN10 filter, which are approximately 1 mm long.

5.4.2 Transmittance of the H-continuum filters

To asses the transmittance of the H-cont witness sample and filters, under different temperatures, the transmittance of one witness sample was measured at 293 K, 100 K and 84 K. Again, we will focus on analyzing the behavior of the transmission windows at 84 K. The transmission spectrum of the H-continuum witness sample is shown in Figure 5.18 and the most prominent feature is a small dip in the transmittance at around 1580 nm. However, it is

of no concern, since the average transmission of the data points above the 90% requirement is equal to 92.63%. Again, we observe a decrease in transmittance at the top of the curve when the temperature is reduced from 293 K to 84 K. For the H-continuum witness sample, this difference was quantified to be 1.78% and it can be attributed to the same reasons mentioned for the [FeII] sample in subsection 5.3.2. We have also determined that the transmission window of the sample shifted by 1.90 nm to shorter wavelengths at 84 K (see Figure 5.19).

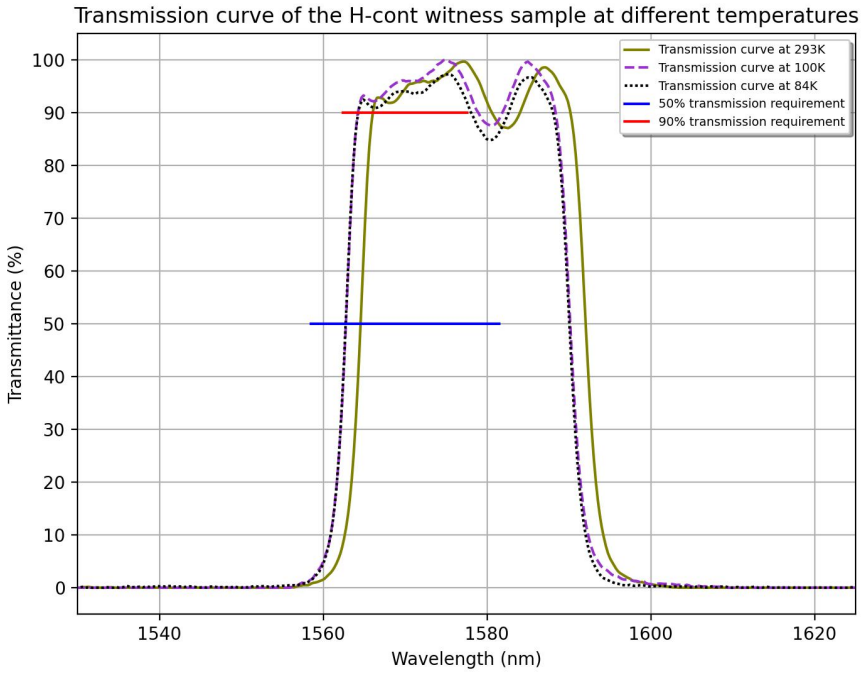

Figure 5.18: Comparison of the transmission spectra of the H-continuum witness sample at 293 K, 100 K and 84 K. The red and blue horizontal lines indicate the regions where the transmission has to be larger than 90% and 50%, respectively.

The same statistics used to analyze the [FeII] filters and sample, was applied to the H-cont data sets. The maximum value that the CWL of the filters and of the witness sample can deviate from the theoretical CWL (1570 nm) is 4.71 nm. It was determined that the CWL of the witness sample at 84 K is shifted by 6.31 nm towards longer wavelengths from the theoretical CWL value, meaning that it is not compliant. Again, the H-cont SN10 and H-cont SN18 filters data provided by Cilas was taken at room temperature, so the sample's thermal shift of 1.90 nm was subtracted from the wavelength values of the filters. Afterwards, we computed their CWL and we found that the SN10 filter meets the specification. However, the CWL of the H-cont SN18 filter deviates by 5.33 nm from the theoretical CWL, making it not compliant. Since the H-cont filter will be used to look at a line free region, the deviation from the CWL will not affect its performance and it will most likely be accepted.

A plot of the transmission curves of the two H-cont filters at 84K is depicted in Figure 5.20. It can be seen that the 50% and 90% transmission requirements fall well within the transmis-

sion region. The small dip at around 1580 nm is less prominent in the SN18 filter, while the SN10 filter shows a flatter transmission peak between 1560 nm and 1580 nm. The ringing of the witness sample at 84K is 3.70%, which, similarly to the [FeII] filter, can be explained by the presence of a dip in transmittance, this time located at 1580 nm. The filters' ringing is smaller than the value for the sample, but it is still above the 2% requirement, as for the [FeII] filters. A more detailed overview of all the results is presented in Table 5.4.

After removing the witness sample out of CRiSP, it was inspected in the laminar flow cabinet and no new defects were noticed on its surface. This confirms that the coating and the substrate endured the cryogenic cycle, meaning that the filters will also perform well at very low temperatures. Thus, the H-continumm SN10 filter is to be used in the MICADO's pupil wheel based on the observations of its transmission window measurement, while the SN18 filter will serve as a spare.

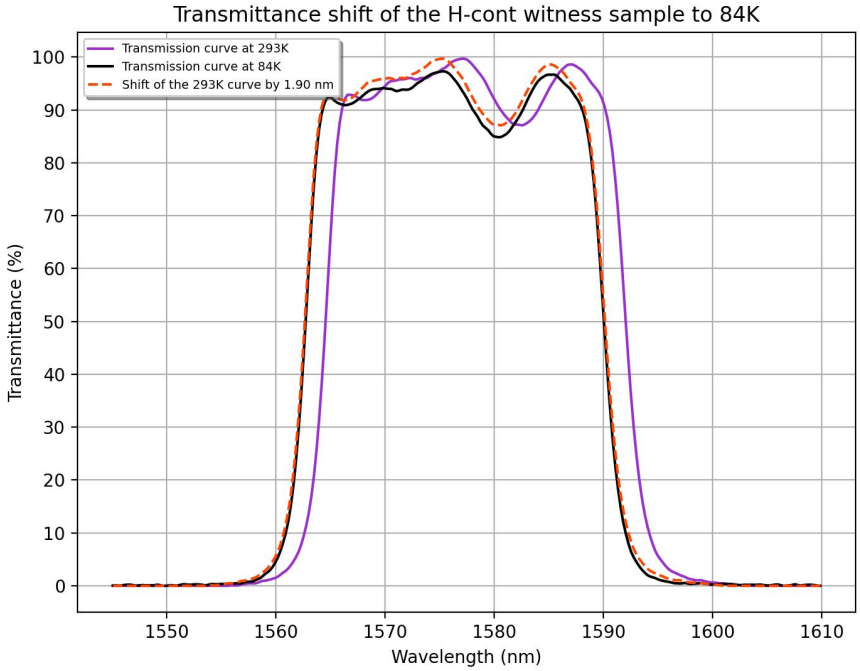

Figure 5.19: The reference transmission curve of the H-continuum witness sample measured at 293 K (in purple) was shifted by 1.90 nm with respect to the measured transmission spectrum at 84 K. The shift was obtained by minimizing the root sum squared difference between the two measured spectra.

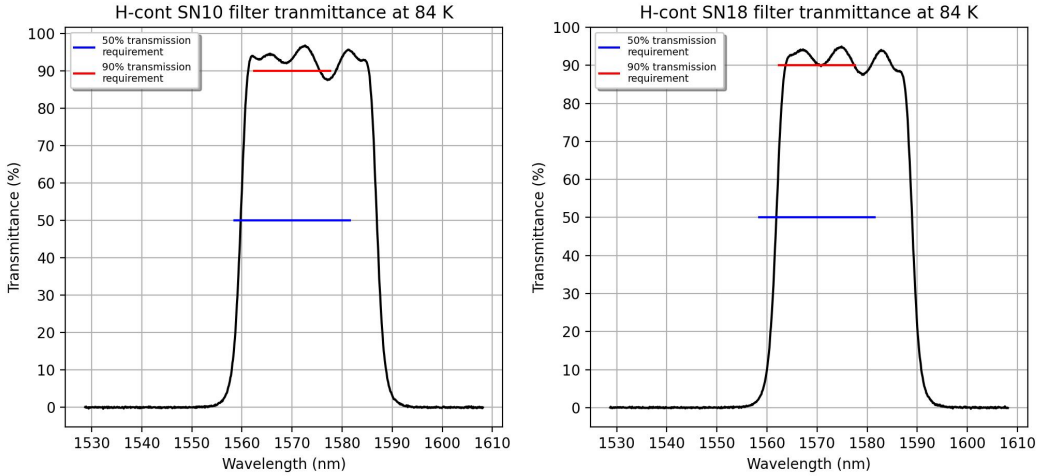

Figure 5.20: The transmission curves of the two H-cont filters after applying a shift of 1.90 nm to their wavelength values. This is an approximation of how the bandpass region would look at a temperature of 84 K. The original data has been provided by Cilas and it was collected at room temperature.

Table 5.4: Summary of the measured parameters for the H-cont filter requirements.

Filter	**Theoretical CWL**	**CWL at 293K**	**CWL at 84K**	**Shift from theoretical CWL**	**Maximum allowed shift**	**Ringing**	**Compliance**
H-cont sample	1570.0 nm	1578.24 nm	1576.31 nm	6.31 nm	4.71 nm	3.70%	No
H-cont SN10		1575.21 nm	1573.31 nm	3.31 nm		2.69%	Yes
H-cont SN18		1577.23 nm	1575.33 nm	5.33 nm		2.54%	No

5.5 The I-long filter

The coating of the two I-long filters and the corresponding witness samples was carried out by SCHOTT in Switzerland. These filters are larger than the narrow-bands and measure 145 mm in diameter, while their thickness is 10 mm. The coating was applied on an Infrasil 302 substrate. The witness samples have a diameter of 25 mm and are 10 mm thick. The samples have visible defects around the edge since they were cut from a larger blank. One of them was cut from the center of the blank and is marked by letter C, while the other was taken from a region closer to the edge of the blank and is labeled with letter M (see Figures 7.7 to 7.9 in the Appendix).

5.5.1 Visual inspection of the I-long filters

The two I-long filters have a large number of defects on their surfaces. These defects come from small particles of coating breaking off the distribution mask in a sputtering-down machine. As the coating process took two days, the material buildup on the distribution mask increased, leading to the defects that we observed. SCHOTT reported 34 defects on face 1 of the I-long 8537-01 filter, and 46 defects on face 1 of the I-long 8537-13 filter, as seen in Figure 5.21.

Since the number of defects present on the surface was overwhelmingly large (see Figure 5.22), we decided to focus only on those visible to the naked eye. For instance, the defects marked by the numbers 5-9 from face 2 of the I-long 8537-13 filter, could be clearly seen under good light without the need to zoom-in on them (see Figure 5.23). Both filters exhibit scratch like patterns as depicted in Figure 5.24. However, under maximum microscope magnification, these patterns were revealed to be closely spaced dots, with an example presented in Figure 5.25.

Unfortunately, having such a large number of defects, makes it impossible to predict the effects of stray light on the performance of the filter, which could raise the background level in observations. This, in turn, would make it more difficult to perform photometry and high contrast imaging in the I-band. Hence, it was decided to reject these filters and ask SCHOTT to re-do the coating using using a sputtering-up machine that will reduce the chance of particles being deposited in the coating.

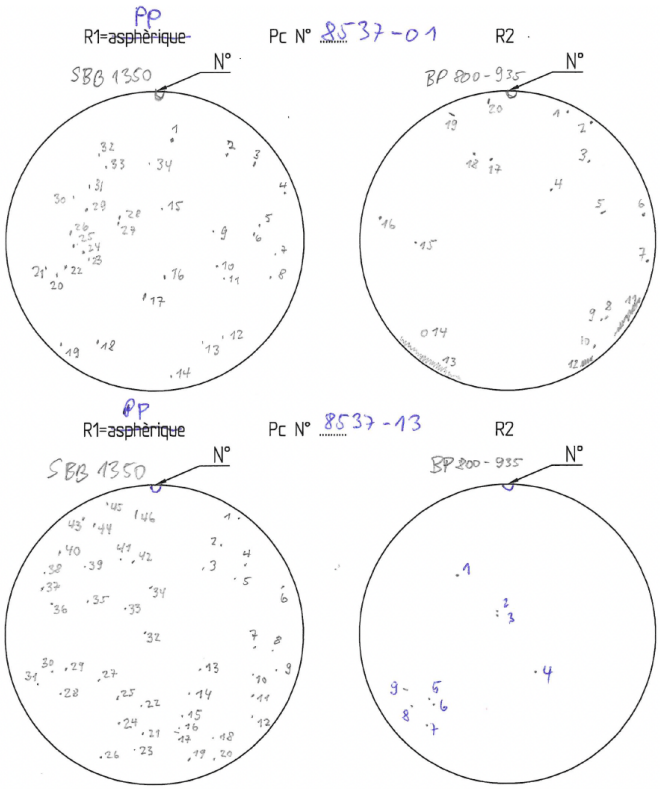

Figure 5.21: The defects map provided by SCHOTT for the two I-long filters. The company marked 34 defects on face 1 of the I-long 8537-01 filter (upper left) and 46 defects on side 1 of the I-long 8537-13 filter (lower left). The second face of both filters show considerably less defects.

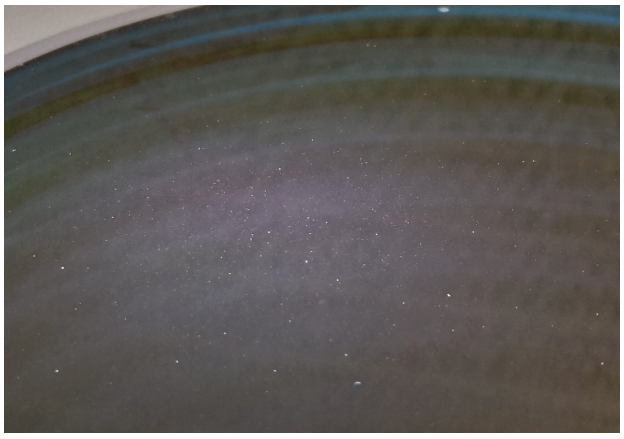

Figure 5.22: A zoom-in on face 2 of the I-long 8537-01 filter. Multiple coating defects can be seen as small, white dots.

Figure 5.23: The defects marked by SCHOTT as numbers 5, 6, 7, 8, 9 in Figure 5.21, in the lower left part of the I-long 8537-13 filter on face 2.

Figure 5.24: Defect in the shape of a line on face 2 of the I-long 8537-01 filter and marked by SCHOTT as number 5 in Figure 5.21.

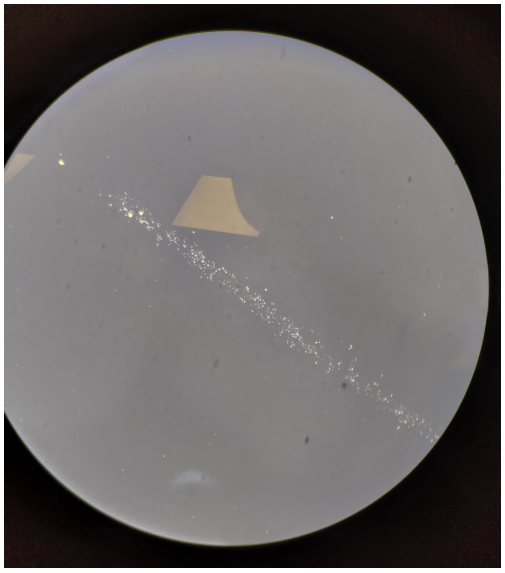

Figure 5.25: Defect number 5 from face 2 of the I-long 8537-01 filter at maximum zoom through the microscope. It is a stripe of dots clustered very closely together and it measures approximately 3 mm in length.

5.5.2 Transmittance of the I-long witness sample

Even though these filters were rejected, it is still useful to check their transmittance. Unfortunately, SCHOTT did not provide the measured data for the two I-long filters taken at room temperature. Hence, we will only discuss one of the witness samples in this subsection.

For this analysis, the I-long witness sample cut from the edge of the larger blank was chosen, since the coating thickness and deposition quality can vary more near the edges. Note that the following results are for an angle of incidence (AOI) of 0°, while the actual filter will be placed at a tilt of 3.75° in MICADO's filter wheel. As seen in Figure 5.26, even with a large number of surface defects, both the 50% and 90% transmission requirements are met. When comparing it to the previously described narrow-band filters, the top of the I-long sample is flatter and the shift of the overall transmission region from room temperature to 84 K is only 0.99 nm (see Figure 5.28). This shift is smaller for the I-long witness sample and it may be due to the presence of a thicker coating on the substrate and the use of a different coating material compared to the [FeII] and H-cont filters. Moreover, based on the analysis done by van den Born et al., 2024 on three samples provided by SCHOTT in late 2024, there appears to be a trend suggesting that the transmission window shift at cryogenic temperatures is smaller at shorter wavelengths. As the I-long filter is on the shorter wavelength side, compared to the [FeII] and H-continuum filters, the above mentioned trend could apply.

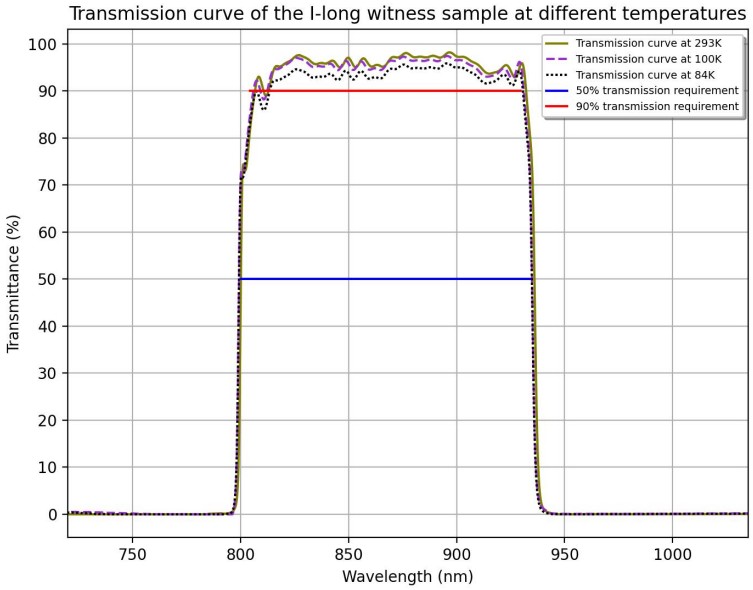

Figure 5.26: Comparison of the transmission spectra of the I-long witness sample at 293 K, 100 K and 84 K. The red and blue horizontal lines indicate the regions where the transmission has to be larger than 90% and 50%, respectively.

The decrease in transmittance from 293 K to 84 K was computed to be 2.43%, which is larger than the difference observed in the two witness samples previously analyzed. The big number of defects in the coating may cause scattering, blockage or absorption of light, leading to a decrease in transmittance at lower temperatures due to the shrinkage of the coating's layers. However, further investigation is needed to draw a conclusion.

After performing the data analysis process, the CWL of the witness sample at 84 K, was determined to be 864.15 nm, which deviates from the theoretical CWL by 2.85 nm. The maximum allowable deviation of the broadband filters' CWL is defined as 0.5% of the theoretical CWL, and it is equal to 4.33 nm for the I-long. So, it can be concluded that the I-long sample is compliant. Since the transmission region above 90% is much flatter for this sample, the ringing was calculated to be 2.45%, which is close in value to the desired 2%.

In order to quantify how the angle of incidence will influence the filters, an older design proposed by SCHOTT was used, since this was the only available file with consistent data at multiple AOI values. Note that it is not entirely representative of the final design and it went through an update. This data set includes wavelength and transmittance values at AOI of 0° and 8°, which were used to determine an effective refractive index of the coating. Reordering Equation 2.12, we obtain

$$n = \sqrt{\frac{\sin^2\theta}{1-(\frac{\lambda_\theta}{\lambda_0})^2}}. \tag{5.5}$$

By taking the transmission weighted average of the wavelength, it was found that $\lambda_0 = 873.09$

for $\theta = 0°$ and $\lambda_\theta = 870.06$ nm when $\theta = 8°$. Based on this wavelength shift, the refractive index of the coating was determined to be 1.75 ± 0.29. Next, Equation 2.12 was employed using $\lambda_0 = 864.15$ nm, which represents the CWL of the I-long sample at 84 K and $\theta = 3.75°$, yielding a central wavelength $\lambda_\theta = 863.55 \pm 0.21$ nm. Therefore, an extra 0.6 nm shift to shorter wavelengths is introduced due to the nominal filter tilt of 3.75°, which is expected from theory. As seen in Figure 5.29, the sample's curve still satisfies the 50% and 90% transmission requirements and it complies with the CWL shift specification. The other witness sample yielded similar results, from which we can conclude that the coating was applied uniformly both at the center and at the edge of the blank.

Another interesting case that we analyzed is the variation of the transmission across MICADO's field of view (FoV). As depicted in Figure 5.27, the light passing through the edge of the I-long filter, will be incident at an angle of ±3.5° with respect to the vertical axis. Thus, the final AOI of the light beam on the left is equal to 0.25°, while on the right it is 7.25°. By applying Equation 2.12, the CWL of the witness sample will be located at 861.91 nm when $\theta = 7.25°$ and it will not be compliant. However, since I-long is a broad-band filter, this minor shift towards shorter wavelengths will not influence the observations. By repeating the same calculation for $\theta = 0.25°$ on the witness sample, we obtain a CWL of 864.15 nm, which coincides with the CWL measured at the 0° angle.

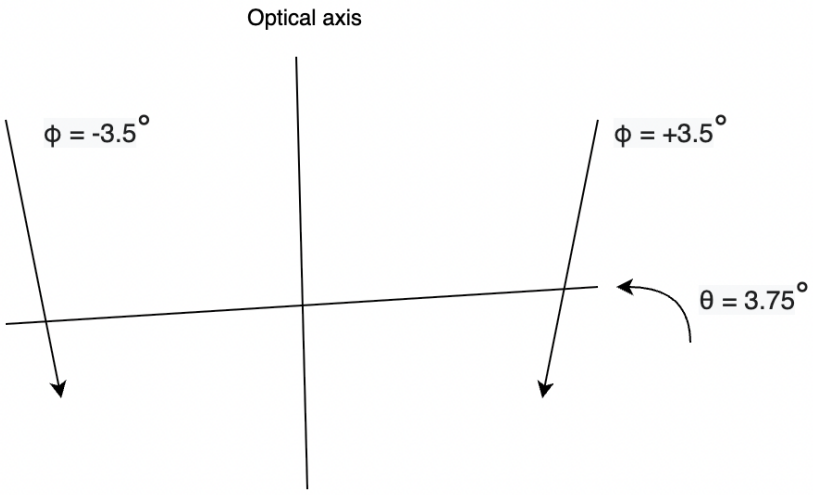

Figure 5.27: Sketch of the variation in the AOI across MICADO's FoV. The I-long bandpass filter is at a tilt of $\theta = 3.75°$ in the filter wheel of MICADO. The incident light at the edge of the filter arrives at an angle $\phi = \pm 3.5°$ with respect to the optical axis. This results in an AOI on the filter surface that ranges from 0.25° to 7.25° across the FoV.

Thus, based on the observations made on the witness samples, we can conclude the filters could be accepted, but, as mentioned previously, the defects on the coating could pose a threat to photometry due to the stray light effects, which led to their rejection.

After removing the witness samples from CRiSP and performing a visual inspection, we

noticed that the one marked with letter C had a scratch on the surface that was caused by the spring used to hold it in place inside the slot (see Figure 7.10). Otherwise, no new defects were observed, from which we can conclude that the filters will withstand operating at cryogenic temperatures.

Table 5.5: Summary of the measured parameters for the I-long witness sample requirements.

Filter	Theoretical CWL	CWL at 293K	CWL at 84K	Shift from the theoretical CWL	Maximum allowed shift	Ringing	Compliance
I-long sample	867 nm	865.03 nm	864.15 nm	2.85 nm	4.33 nm	2.43%	Yes

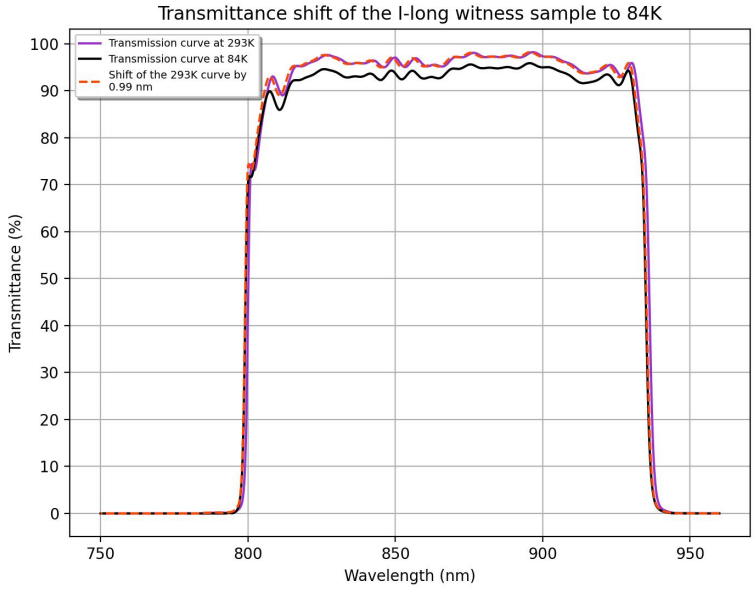

Figure 5.28: The reference transmission curve of the I-long witness sample measured at 293 K (in purple) was shifted by 0.99 nm with respect to the measured transmission spectrum at 84 K. The shift was obtained by minimizing the root sum squared difference between the two measured spectra.

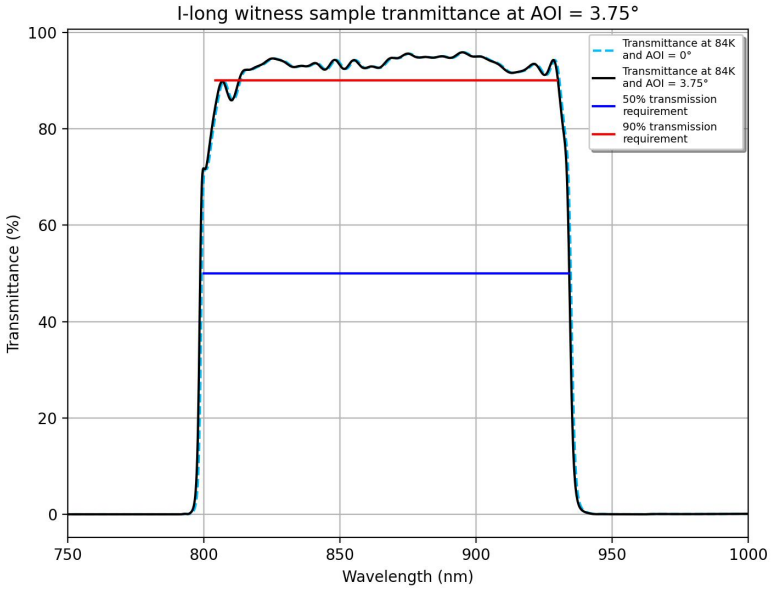

Figure 5.29: Comparison of the transmission window of the I-long witness sample at 84 K at AOI of 0° and 3.5°.

Chapter 6

Conclusions and recommendations

This report presented an overview of the theory behind thin-film coatings and their importance for Astronomy. Such coatings are essential for the optical performance of ELT, which is designed to achieve high sensitivity and resolution across the NIR spectrum with the MICADO instrument. MICADO will feature 27 filters which need to undergo tests to evaluate whether they meet the required specifications. For this thesis, the [FeII], H-continuum, and I-long filters were inspected visually and transmission measurements at room and cryogenic temperatures were performed. After performing the visual inspection, we decided to reject the I-long filters due to the large number of defects in the coating. These defects could lead to scattered light effects, which may negatively impact photometry and high-contrast imaging. The other filters did not show any significant defects in their coatings.

After performing the transmittance measurements on the witness samples at temperatures of 293 K and 84 K, we quantified their thermal shift and used it to estimate the transmission window of the [FeII] and H-continuum filters under cryogenic conditions. We determined that both [FeII] filters are compliant with the transmission requirements mentioned in NOVA's statement of work (Janssen et al., 2024) and hence, any of the two can be integrated in the pupil wheel. The H-continuum SN10 filter was found to comply with the specification, while the H-continuum SN18 filter exceeds the maximum allowed deviation from the theoretical CWL. We arrived to the conclusion that this deviation will pose no threat to the quality of the astronomical observations, as the H-continuum filter will not target a specific emission line. However the H-continuum SN18 filter will be left as a spare and the H-continuum SN10 will be integrated in the pupil wheel. In order to conclude whether we formally accept the [FeII] and H-continuum filters, wavefront error measurements should be performed.

Unfortunately, SCHOTT did not provide files containing the transmission measurements of the I-long filters at room temperature. Thus, no definitive conclusion about their performance can be made. We determined that the sample satisfies all the transmittance specifications regardless of the large number of defects in the coating. Using a past design of the I-long filter made by SCHOTT, we computed the refractive index of the filter's coating to be 1.75 ± 0.29. Since the I-long filter will be integrated in the filter wheel at a tilt of $3.75°$, we found that this angle will lead to an extra shift of the transmission window by 0.6 nm to shorter wavelength in the witness sample. Despite this, the transmittance region is still compliant

with the requirements.

For future work, we recommend to look at detail into the following topics:

- Since, a decrease in the transmission above 80% is noticed at 84 K for all witness samples, it would be useful to perform a detailed error analysis in this region. As the difference in the samples' transmittance at room and cryogenic temperatures is less than 3%, we can roughly estimate that the uncertainties are likely at most 3%.
- It would be advised to request the transmission data files at room temperature for the new set of I-long filters from SCHOTT. This would allow for the wavelength shift measured on the witness sample, to be applied to the filters' data collected at room temperature to estimate the filters' performance in the cryogenic environment.
- Some improvements should be made to the CRiSP cryostat in order to prevent delays when performing measurements of the upcoming filters. A brief overview of the encountered issues and potential solutions on how to solve them are provided in the Appendix.

Bibliography

Argueta, V. (2025, February). Understanding RMS Wavefront Error: An In-Depth Exploration — OFH - Optics for hire. https://www.opticsforhire.com/blog/rms-wavefront-error-explained/

Beckman, J. E. (2021, January). *Infrared Astronomy*. https://doi.org/10.1007/978-3-030-68372-6\{_}3

Brandl, B., Bettonvil, F., Roy, V. B., Glauser, A., Quanz, S., Absil, O., Amorim, A., Feldt, M., Glasse, A., Güdel, M., Ho, P., Labadie, L., Meyer, M., Pantin, E., Hans, V. W., & Consortium, T. M. (2021). METIS: the mid-infrared ELT imager and spectrograph. *arXiv (Cornell University)*. https://doi.org/10.48550/arxiv.2103.11208

Chaturvedi, A., Hilker, M., Cantiello, M., Napolitano, N. R., Van De Ven, G., Spiniello, C., Fahrion, K., Paolillo, M., Gatto, M., & Puzia, T. (2021). The Fornax Cluster VLT Spectroscopic Survey. *Astronomy and Astrophysics*, *657*, A93. https://doi.org/10.1051/0004-6361/202141334

Ciliegi, P., Agapito, G., Aliverti, M., Annibali, F., Arcidiacono, C., Azzaroli, N., Balestra, A., Baronchelli, I., Baruffolo, A., Bergomi, M., Bianco, A., Bonaglia, M., Briguglio, R., Busoni, L., Cantiello, M., Capasso, G., Carlà, G., Carolo, E., Cascone, E., … Xompero, M. (2022). MAORY/MORFEO@ELT: general overview up to the preliminary design and a look towards the final design. *Adaptive Optics Systems VIII*, 40. https://doi.org/10.1117/12.2628969

Corning. (2015). *Corning® HPFS® 7979, 7980, 8655 Fused Silica Optical Materials Product Information* (tech. rep.). https://www.corning.com/media/worldwide/csm/documents/HPFS_Product_Brochure_All_Grades_2015_07_21.pdf

Davies, R., Pott, U., J., & Tolstoy, E. (2022). ELT MICADO: Phase C. MICADO Masks, Stops and Filters Description [Internal revidew document. Doc. No.: ELT-TRE-MCD-56300-0014].

Davies, R., Schubert, J., Hartl, M., Alves, J., Clénet, Y., Lang-Bardl, F., Nicklas, H., Pott, J.-u., Ragazzoni, R., Tolstoy, E., Agocs, T., Anwand-Heerwart, H., Barboza, S., Baudoz, P., Bender, R., Bizenberger, P., Boccaletti, A., Boland, W., Bonifacio, P., … Zins, G. (2016). MICADO: first light imager for the E-ELT. *Proceedings of SPIE, the International Society for Optical Engineering/Proceedings of SPIE*, *9908*, 99081Z. https://doi.org/10.1117/12.2233047

Davies, R., & Sturm, E. (2021). ELT MICADO: Phase C. MICADO Systems Overview [Doc. No.: ELT-TRE-MCD-56300-0064].

Davies, R., Hoermann, V., Rabien, S., Sturm, E., Alves, J., Clenet, Y., Kotilainen, J., Lang-Bardl, F., Nicklas, H., Pott, J.-U., & Tolstoy, E. (2021). MICADO: the Multi-Adaptive

Optics Camera for Deep Observations. *arXiv (Cornell University)*. https://doi.org/10.48550/arxiv.2103.11631

Deep, A., Fiorentino, G., Tolstoy, E., Diolaiti, E., Bellazzini, M., Ciliegi, P., Davies, R. I., & Conan, J.-m. (2011). An E-ELT case study: colour–magnitude diagrams of an old galaxy in the Virgo cluster. *Astronomy and Astrophysics*, *531*, A151. https://doi.org/10.1051/0004-6361/201116603

di Serego Alighieri, S. (1987). Line and continuum imaging. *The Messenger*, *48, p.10-13*.

Dobrowolski, J. (1978). Coatings and filters. In W. Driscoll & W. Vaughan (Eds.), *Handbook of optics* (pp. 8.1–8.124, Vol. 8). Optical Society of America.

Draine, T., Bruce. (2011). *Physics of Interstellar and Intergalactic Medium*. Princeton University Press.

ESO. (2020a). MICADO instrument schematic. Retrieved May 7, 2025, from https://www.eso.org/public/images/instruments-micado-image3/

ESO. (2020b). Artist's impression of the ELT: A sharp eye on the sky. Retrieved May 6, 2025, from https://www.eso.org/public/images/ELT4k-12-Night4-cc/

ESO. (2024). Exploded view of the MICADO instrument. https://www.eso.org/public/netherlands/images/ann24013d/

ESO. (2025). https://elt.eso.org/about/webcams/

Hecht, E. (2017). *Optics*. Pearson.

Hodapp, K. W., Denneau, L., Tucker, M., Shappee, B. J., Huber, M. E., Payne, A. V., Do, A., Lin, C.-C., Connelley, M. S., Varricatt, W. P., Tonry, J., Chambers, K., & Magnier, E. (2020). The outburst of the young star Gaia19bey. *The Astronomical Journal*, *160*(4), 164. https://doi.org/10.3847/1538-3881/abad96

Jacob, R., Schönberner, D., & Steffen, M. (2013). The evolution of planetary nebulae. *Astronomy and Astrophysics*, *558*, A78. https://doi.org/10.1051/0004-6361/201321532

Janssen, A., Navarro, R., & Davies, R. (2021). ELT MICADO: Phase C. ADC Filter and Pupil wheel mechanisms Design and Analysis [Doc. No.: ELT-TRE-MCD-56305-0009].

Janssen, A., Navarro, R., & Davies, R. (2024). ELT-MICADO: Phase D. MICADO Filter coating Specifications and Statement of Work [Internal revidew document. Doc. No.: NOVA-SP-2023-001-MICADO-filter-coating-Specification-and-Statement-of-Work].

Löfdahl, M. G., Henriques, V. M. J., & Kiselman, D. (2011). A tilted interference filter in a converging beam. *Astronomy and Astrophysics*, *533*, A82. https://doi.org/10.1051/0004-6361/201117305

Macleod, A., H. (2001). *Thin-Film Optical Filters*. Institute of Physics Publishing.

Minkina, W. (2021). How Infrared Radiation was Discovered—Range of this discovery and detailed, unknown information. *Applied Sciences*, *11*(21), 9824. https://doi.org/10.3390/app11219824

Morrison, J. (2021). *Modern physics with modern computational methods*. Academic Press.

Muslimov, E. R., Castillo-Domínguez, E., Kariuki, J., Chao-Ortiz, J., Tecza, M., Meyer, E., Ozer, Z., Clarke, F., & Thatte, N. (2024). HARMONI at ELT: Tolerance analysis and expected as-build imaging performance of the infrared spectrograph (J. R. Vernet, J. J. Bryant, & K. Motohara, Eds.), 185. https://doi.org/10.1117/12.3020119

Padovani, P., & Cirasuolo, M. (2023). The Extremely Large Telescope. *Contemporary Physics*, *64*(1), 47–64. https://doi.org/10.1080/00107514.2023.2266921

Paschotta, R. (2019). Standard spectral lines. https : / / doi . org / 10 . 61835 / i46 " title = "Thislinkwillreloadthecurrentpage.

Peatross, J., & Ware, M. (2023). *Physics of light and optics*. Brigham Young University.

Renzini, A., Davies, R., et al. (2009). E-ELT PROGRAMME: MICADO phase A. Scientific Analysis Report [Doc. No.: E-TRE-MCD-561-0007].

Sivia, S., D., & Skilling, J. (2006). *Data Analysis. A Bayesian Tutorial*. Oxford University Press.

Tolstoy, E., & Davies, R. (2018). ELT-MICADO: Phase B. MICADO Science Case [Internal revidew document. Doc. No.: ELT-PLA-MCD-56305-0006].

UQG Optics Ltd. (n.d.). *Suprasil and Infrasil - Material Grades for the Infrared Spectrum* (tech. rep.) (Accessed on 16.06.2025). https : / / www . uqgoptics . com / wp - content / uploads/2019/03/Heraeus-Infrasil.pdf

van den Born, J. (2023). *The MICADO atmospheric dispersion corrector* [Doctoral dissertation, University of Groningen].

van den Born, J., Aranzana, E., & Kwast, S. (2024). Cryogenic transmission measurement of three filters at $40K$, $82K$, $100K$ and $293K$ [Internal review document. Doc. No.: NOVA-RP-2024-015].

Vidal, F., Galland, N., Bertrou-Cantou, A., Gendron, É., Deo, V., Zidi, A., Ferreira, F., Sevin, A., Kulcsár, C., Raynaud, H.-F., Clénet, Y., & Davies, R. (2022). The MICADO first light imager for the ELT: FDR numerical simulations for the SCAO mode. *Adaptive Optics Systems VIII*, 214. https://doi.org/10.1117/12.2629308

Welch, C. A., Frank, A., Pipher, J. L., Forrest, W. J., & Woodward, C. E. (1999). [FeII Bubbles in the Young Planetary Nebula Hubble 12. *The Astrophysical Journal*, *522*(1), L69–L72. https://doi.org/10.1086/312206

Yi, S., Demarque, P., Kim, Y.-C., Lee, Y.-W., Ree, C. H., Lejeune, T., & Barnes, S. (2001). Toward better age estimates for stellar populations: the Y 2 isochrones for solar mixture. *The Astrophysical Journal Supplement Series*, *136*(2), 417–437. https://doi.org/10.1086/321795

Acknowledgments

During the past 3 months, I gathered an enormous amount of experience not only in mastering theoretical and practical aspects of instrumentation, but also in working effectively as part of a team. I would like to thank Joost van den Born for the time and effort he put throughout this project. Despite his busy schedule, he always made space to guide and help me during challenging moments. I am equally grateful to Ester Aranzana for ensuring that everything stayed on track throughout my internship. Her valuable input on my writing and the advice she gave me on approaching various problems and improving my work, were incredibly helpful. During the moments when I was drifting too far from Astronomy, the meetings with Eline Tolstoy always helped me find ways to connect my research to the field. A special thank you goes to Eddy Elswijk, who spent a week helping me repair CRiSP. This bachelor project would have been impossible without him. Last, but not least, I want to thank everyone else in the NOVA Dwingeloo group for their help, advice and the nice moments we shared both during and outside the working hours.

My friends also played an important role in supporting me throughout this journey. I appreciate the time and effort that Bartosz Strent and Ot Roof invested into helping me with parts of the data analysis code. And, of course, the thesis writing sessions with Geralt Wawrzynkiewicz-Raźny made me feel not alone throughout the past weeks.

AI tools usage

Throughout this report, AI tools have been used to format Table 4.1 and generate LaTeX codes for inserting figures. Sometimes, AI was employed for suggesting ideas on how to rephrase my own writing when the same words were repeated too often and I could not find suitable synonyms or think of creative ways to reshuffle my thoughts. Last, the AI tools helped debug some of the code that I wrote myself. The only fully generated AI script is the one for reading the .csv files provided by Cilas, since they had an unusual structure. None of the data used in this report was uploaded to any AI system.

Appendix

Measurement logs

Table 7.1: The pressure and temperatures read from multiple sensors attached inside CRiSP.

Date	Pressure (mbar)	Cold head temperature (K)	Shield temperature (K)	Sample temperature (K)	Wheel temperature (K)
16.06.2025	$3{\cdot}10^{-4}$	295.269	294.925	293.649	293.444
17.06.2025	$2.8{\cdot}10^{-4}$	69.677	101.788	84.247	81.146
18.06.2025	$2.7{\cdot}10^{-4}$	97.135	105.394	101.266	99.544
23.06.2025	$6.6{\cdot}10^{-4}$	295.453	295.182	293.874	293.697

Raw data and data processing

The data collected in this test campaign along with the Python script used to perform the analysis can be found in the following Google drive link:
https://drive.google.com/drive/folders/1ripmTF9BpH3RR0Syn5lap5o8WVqnFtKn?usp=drive_link

The simulation of a thin film filter from chapter 2 is stored in the drive with the link below:
https://drive.google.com/drive/folders/1su6dXLSog46366b8CWTBaW2jJ9ufAcVW?usp=drive_link

The background measurements

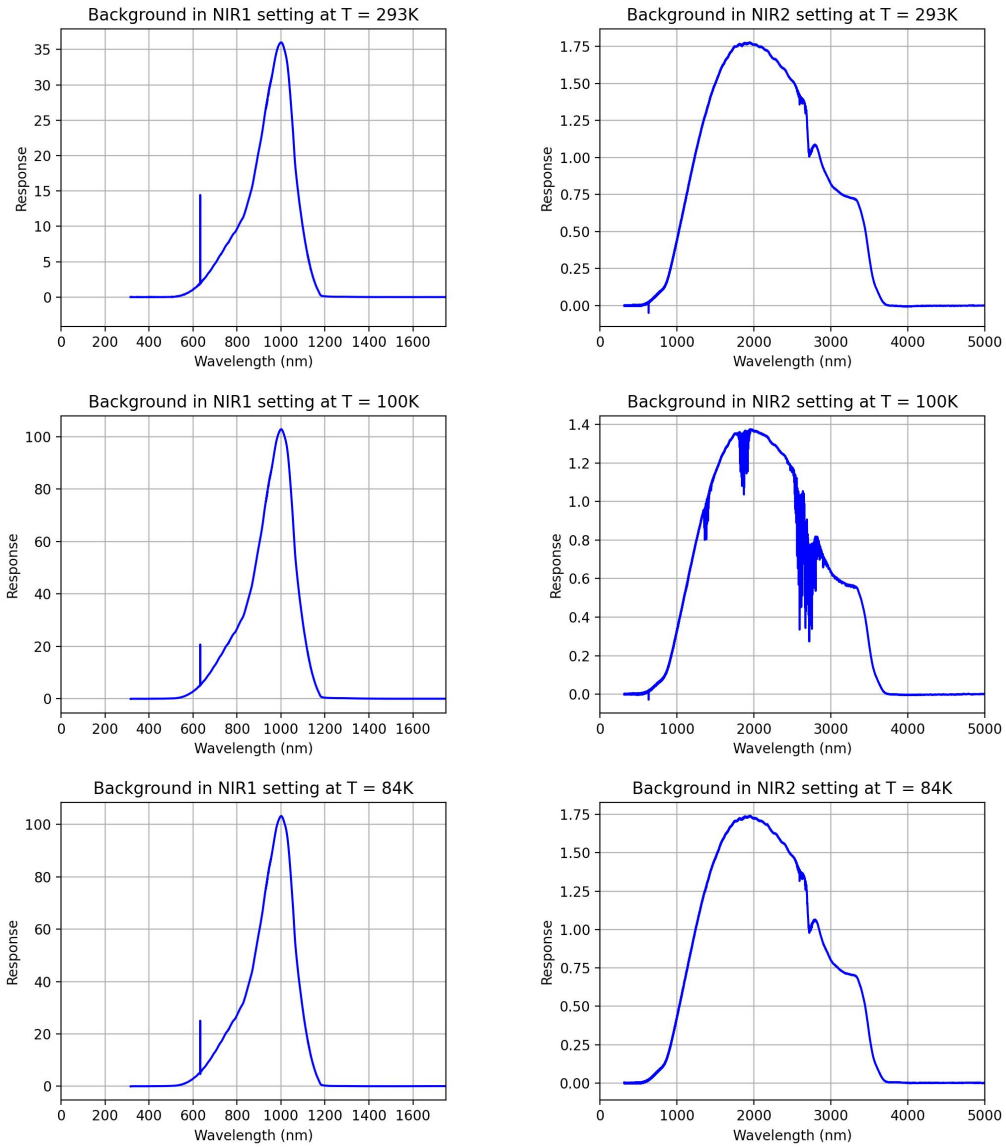

Figure 7.1: The backgrounds taken with the NIR1 and NIR2 settings of the spectrometer at 84K, 100K and 293K. The emission line of the HeNe laser of the spectrometer can be see at 632.87 nm.

[The FeII] witness samples

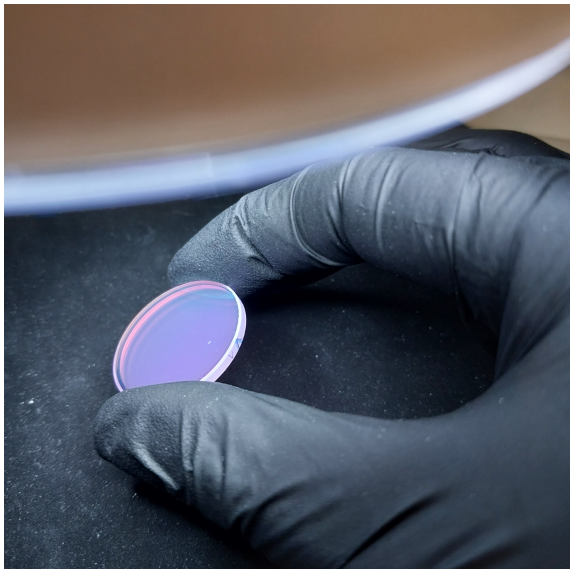

Figure 7.2: The [FeII] witness sample 252 B140/142, 132a. This is the witness sample used in the transmission test campaign.

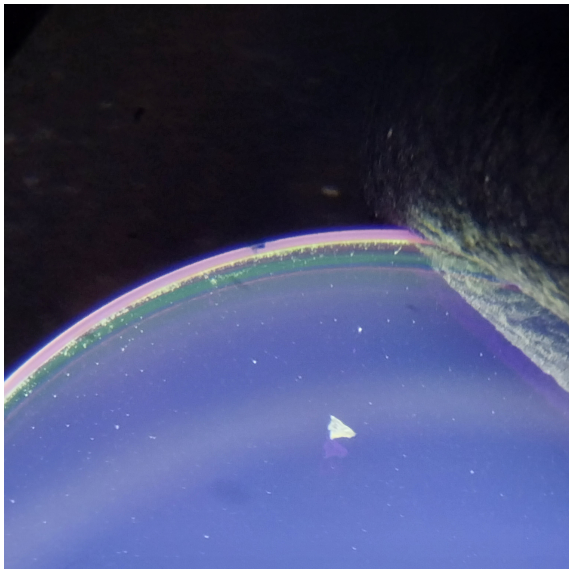

Figure 7.3: Defect in the coating of the [FeII] witness sample 252 B140/142, 132a.

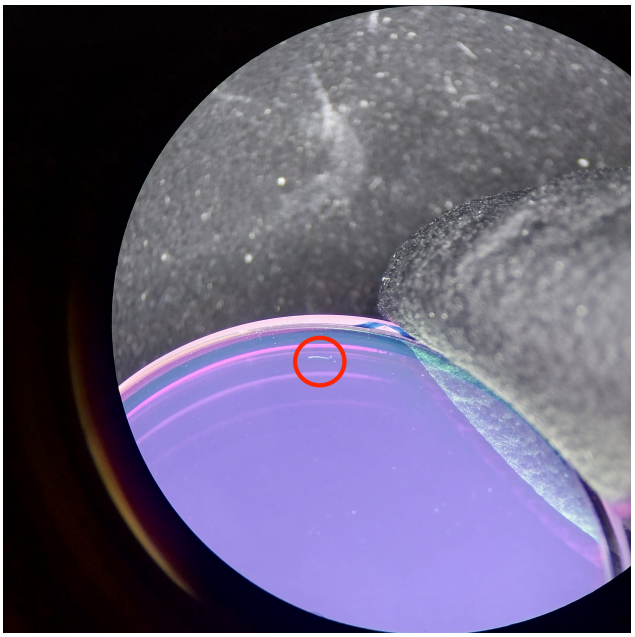

Figure 7.4: Defect in the coating of the [FeII] witness sample 252 B140/142, 332a.

The H-cont witness samples

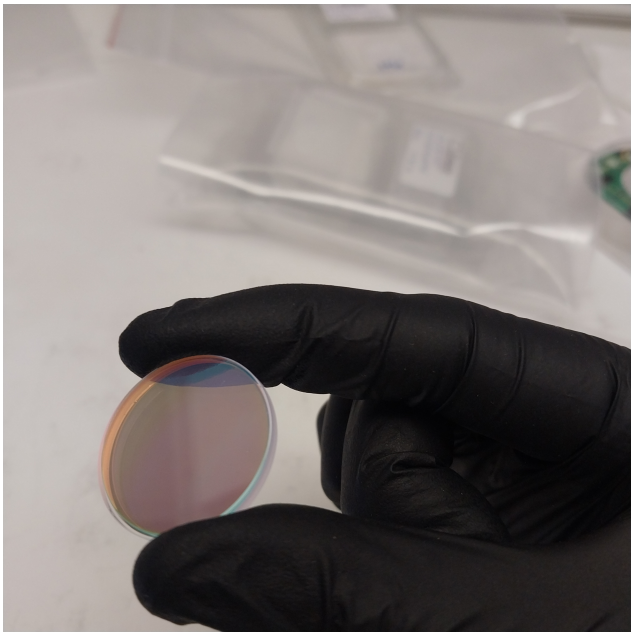

Figure 7.5: The H-cont witness sample 252 B140/142, 211f. No defects were found in its coating.

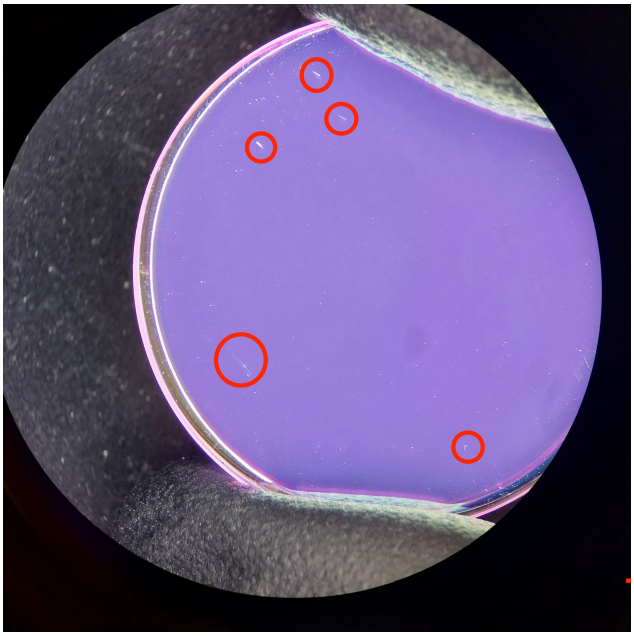

Figure 7.6: Defects in the coating of the H-cont witness sample 252 B140/142, 211a. This is the sample used in the test campaign.

The I-long witness samples

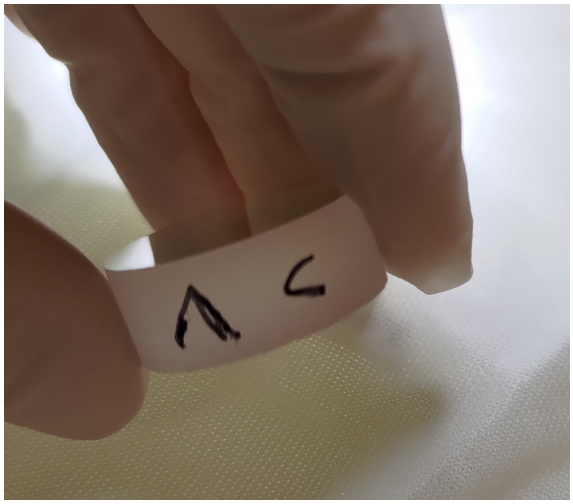

Figure 7.7: The I-long witness sample cut from the center (C) of a 145 mm diameter blank.

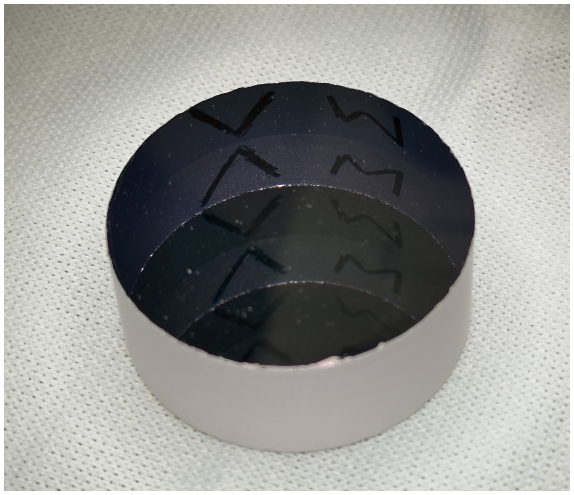

Figure 7.8: The I-long witness sample cut from the edge (M) of a 145 mm diameter blank.

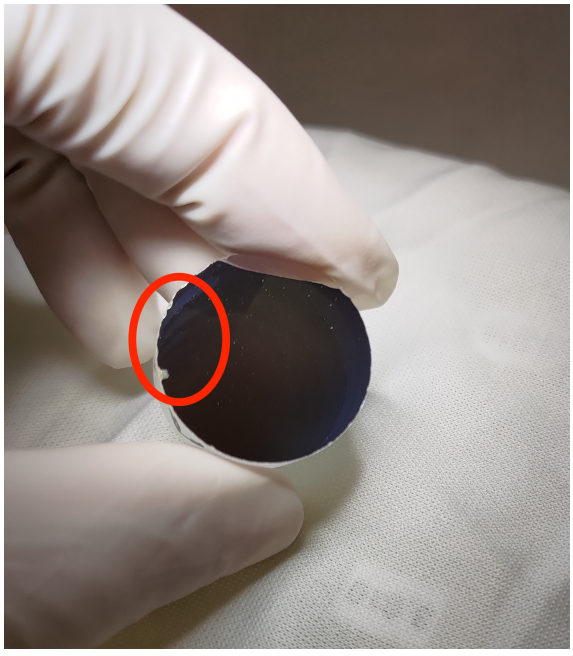

Figure 7.9: An example of the defects present at the edge of the I-long witness samples due to being cut from a larger blank.

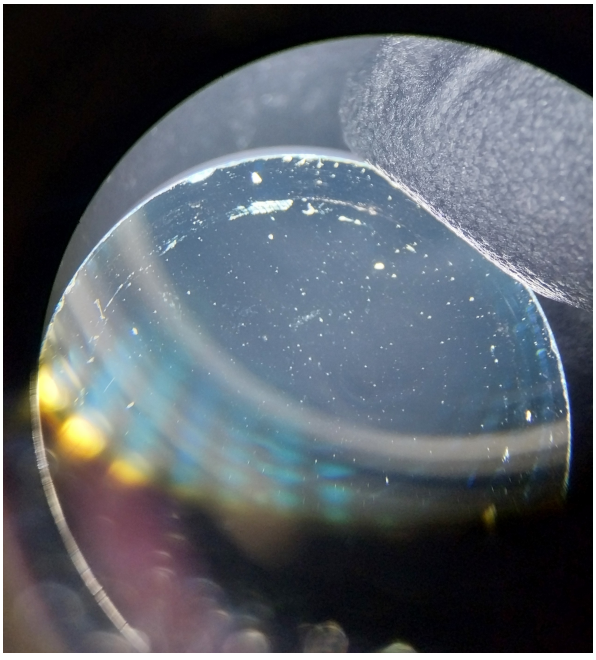

Figure 7.10: The damage cause by the spring used to fix the I-long witness sample C in place inside the slot number 6 of CRiSP.

Transmission window shift at the temperature of 100K

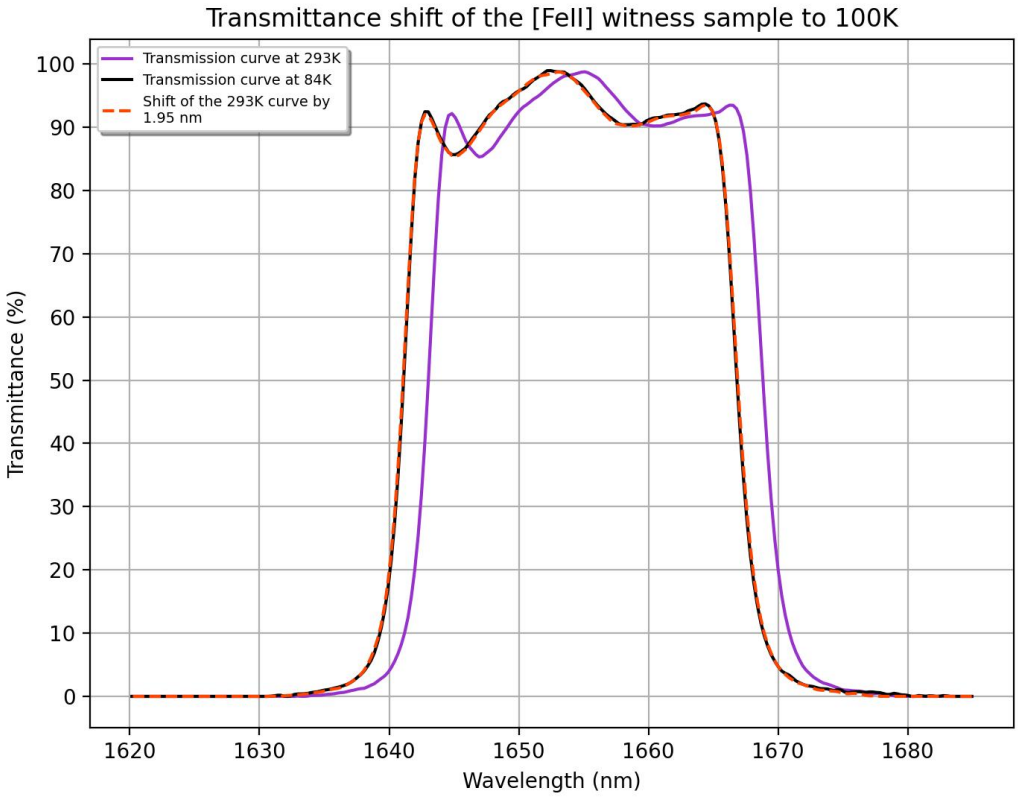

Figure 7.11: The reference transmission curve of the [FeII] witness sample measured at 293 K (in purple) was shifted on top of the measured transmission spectrum at 100 K. The shift was obtained by minimizing the root sum squared difference between the 2 measured spectra and it has a value of 1.95 nm. The CWL of the transmission window at 100 K is 1653.99 nm.

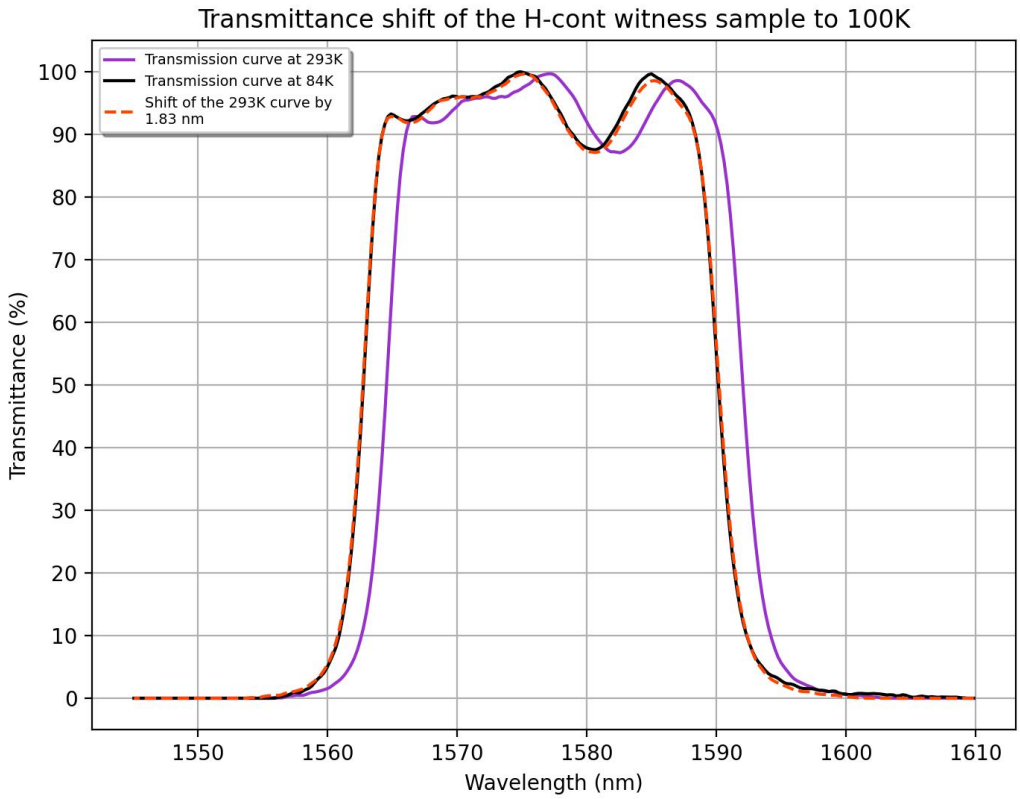

Figure 7.12: The reference transmission curve of the H-continuum witness sample measured at 293 K (in purple) was shifted on top of the measured transmission spectrum at 100 K. The shift was obtained by minimizing the root sum squared difference between the 2 measured spectra and it has a value of 1.83 nm. The CWL of the transmission window at 100 K is 1576.50 nm.

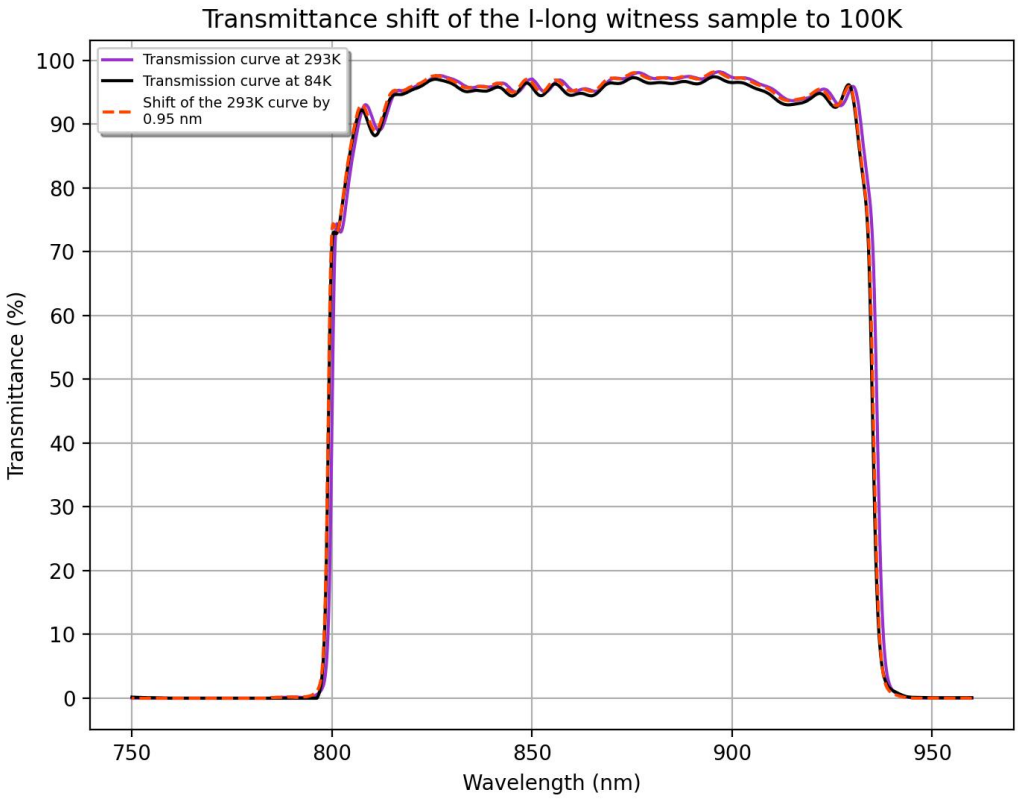

Figure 7.13: The reference transmission curve of the I-long witness sample measured at 293 K (in purple) was shifted on top of the measured transmission spectrum at 100 K. The shift was obtained by minimizing the root sum squared difference between the 2 measured spectra and it has a value of 0.95 nm. The CWL of the transmission window at 100 K is 864.10 nm.

Error analysis of the refractive index

In order to find the error in the refractive index of the coating of the I-long filter and its witness samples, the partial derivative of the expression given by Equation 5.5 was taken with respect to λ_θ, since it is the only parameter that deviates from a true theoretical value. Its error is taken to be the difference between the theoretical CWL of 867 nm and the calculated CWL for the I-long filter transmission simulated for an AOI = 8°, which is 870.06 nm. We found that this difference is equal to 3.06 nm. The expression for computing the uncertainty in the refractive index is given by

$$\Delta n = \sqrt{\left(\frac{\partial n}{\partial \lambda_\theta}\Delta\lambda_\theta\right)^2} = \frac{|\sin(\theta)|\,\lambda_\theta}{\lambda_0^2\left(1-\frac{\lambda_\theta^2}{\lambda_0^2}\right)^{3/2}}, \tag{7.1}$$

where $\theta = 8°$ and λ_0 is the CWL of the simulated I-long filter at the AOI of 0° and it is equal to 873.09 nm. After performing the computations, the refractive index of the coating can be written as $n = 1.75 \pm 0.29$. The partial derivative was performed using an online calculator.

Having computed the refractive index error, it is possible to find the uncertainty in the CWL of the I-long witness sample by taking the partial derivatives of Equation 2.12 with respect to $\lambda_0 = 864.15$ nm being the CWL of the witness sample at AOI of 0°, and $n = 1.75$ as

$$\Delta\lambda_\theta = \sqrt{\left(\frac{\partial\lambda_\theta}{\partial\lambda_0}\Delta\lambda_0\right)^2 + \left(\frac{\partial n}{\partial\lambda_0}\Delta n\right)^2} = \sqrt{\left(\sqrt{1-\frac{\sin^2\theta}{n^2}}\;\Delta\lambda_0\right)^2 + \left(\frac{\sin^2\theta\;\lambda_0}{n^3\sqrt{1-\frac{\sin^2\theta}{n^2}}}\;\Delta n\right)^2}. \tag{7.2}$$

In the above equation, $\Delta\lambda_0 = 0.07$ nm, while $\Delta n = 0.29$. After performing the computations, the uncertainty in the CWL of the I-long witness sample is $\Delta\lambda_\theta = 0.21$ at the angle of incidence of 3.75°.

A failure in one of CRiSP's components

While integrating the witness samples in CRiSP on the 4th June 2025, we noticed that the sample wheel was wobbling when rotating and it became tilted at an angle. Between the 5th and the 13th of June, with help from Eddy Elswijk, I spent time looking for the cause and ways to solve it. We found that the piece that connects to the thermal strap behind the sample wheel got twisted (see Figure 7.14). The thermal strap winds around the piece in question as the motor rotates the sample wheel. This caused the thermal strap to get stuck in one of the regions marked in red in Figures 7.15 and 7.16. Two new pieces were manufactured and one of them was installed in CRiSP, while the other is stored as a spare. Before attaching the sample wheel back, the thermal strap was stretched by hand to bring back its elasticity temporary. However, we recommend that before the next testing round, a piece of stainless steel spring be glued to the thermal strap to ensure it does not get stuck anymore. We were unable to implement this solution before this testing campaign, because no suitable stainless steel springs were available in the workshop.

Figure 7.14: The component that got twisted because the thermal strap kept getting stuck, which required extra force to be applied on this piece whenever the motor rotated.

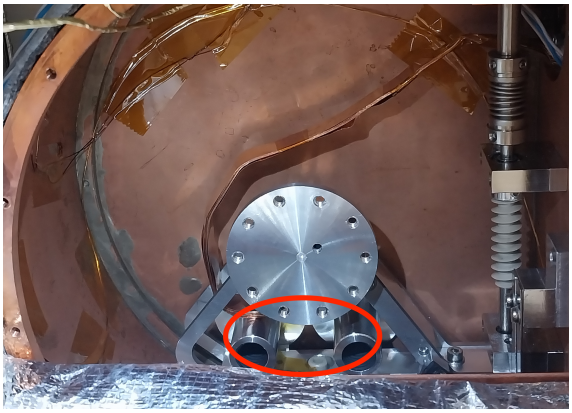

Figure 7.15: One of the two regions where the thermal strap would get stuck.

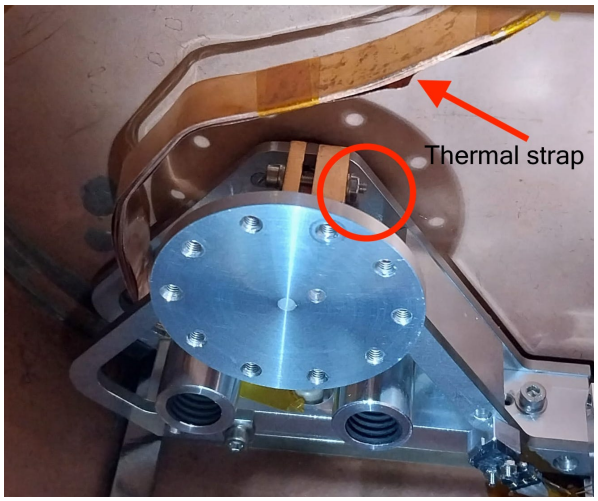

Figure 7.16: The second region where the thermal strap would get stuck (red circle). The thermal strap can also be clearly seen and it is indicated by the red arrow.